

Rapid Microfluidic Double-Jump Mixing Device for Single-Molecule Spectroscopy

Fabian Dingfelder,[†] Bengt Wunderlich,[†] Stephan Benke,[†] Franziska Zosel,[†] Niels Zijlstra,[†] Daniel Nettels,[†] and Benjamin Schuler^{*,†,‡,§}

[†]Department of Biochemistry, University of Zurich, Winterthurerstrasse 190, 8057 Zurich, Switzerland

[‡]Department of Physics, University of Zurich, Winterthurerstrasse 190, 8057 Zurich, Switzerland

Supporting Information

ABSTRACT: We introduce a microfluidic double-jump mixing device for investigating rapid biomolecular kinetics with confocal single-molecule spectroscopy. This device enables nonequilibrium dynamics to be probed, e.g., transiently populated intermediates that are inaccessible with existing single-molecule approaches. We demonstrate the potential and reliability of the method on time scales from milliseconds to minutes by investigating the coupled folding and binding reaction of two intrinsically disordered proteins and the conformational changes occurring in a large cytolitic pore-forming toxin.

Single-molecule fluorescence spectroscopy has become a key methodology for the investigation of biomolecular mechanisms. A particular strength is the possibility to extract information on complex kinetics and dynamics over a broad range of time scales, both in equilibrium and nonequilibrium experiments.^{1–5} Perturbation techniques are required in cases where the molecular species of interest are not populated to a detectable degree at equilibrium. Microfluidic mixing coupled to single-molecule detection is a powerful technique for investigating such biomolecular processes under nonequilibrium conditions,^{6–9} with dead times in the low millisecond range^{7,9} or even below.⁸ A promising extension of rapid mixing is the double-jump mixing technique, which is well established for ensemble experiments based on stopped-flow mixing:^{10,11} by enabling the transient population of unstable reaction intermediates, it allows their role in kinetic mechanisms to be probed. However, no such approach has been available for investigating kinetics with single-molecule resolution. Here we present a microfluidic device that is optimized for performing two consecutive rapid mixing steps separated by a well-defined delay time. In this way, a first change in solution conditions is employed to populate an unstable intermediate species, and a second mixing step to probe its kinetic properties. We demonstrate the versatility of this double-jump device with two examples occurring on very different time scales: (i) the association and dissociation of a protein complex on the millisecond time scale in a single experiment, and (ii) the kinetic investigation of an intermediate state in the conformational reorganization of a pore-forming toxin from milliseconds to minutes.

The design of the device (Figure 1a) is based on laminar flow and diffusive mixing¹² and was optimized for the desired mixing

ratios and flow velocities using 3D finite-element calculations (Figure S1). The first rapid mixing step with a dead time of ~10 ms is followed by a delay channel whose length is optimized for the formation of the intermediate of interest. After the second mixing step, two additional pairs of outlet channels perpendicular to the observation channel were introduced. The effect of the resulting diverted flow is 2-fold: (1) The flow is rapidly decelerated to velocities compatible with confocal single-molecule detection,¹³ thus decreasing the dead time to ~7 ms, and (2) the even slower flow in the wider side outlet channels allows observation times of up to 5 min (Figure 1b), thus enabling a broad range of time scales to be investigated in a single device. The conformational changes of the sample molecules can be followed by confocal detection at various positions along the observation channel or in the side outlet channels. To obtain reliable devices with stable flow patterns and highly reproducible mixing behavior, we use microfabrication based on reactive ion etching in silicon for producing device molds with high accuracy in the resulting structures, essential in particular for the narrow channels that enable fast diffusive mixing with millisecond dead time (Figure 1c). Combined with replica molding in poly(dimethylsiloxane) (PDMS),¹⁴ large numbers of devices can be generated with great reproducibility and precision (see Materials and Methods), as verified by scanning electron microscopy (Figure 1c and Figure S2). The PDMS devices were bonded to microscope cover glasses after plasma activation (Figure 1d) and interfaced with confocal single-molecule detection via a previously described cartridge-based device holder.⁹ Extensive testing of the flow patterns by wide-field fluorescence imaging (Figure S3) and of flow velocities and mixing ratios by fluorescence correlation spectroscopy (Figures S4 and S5) demonstrates good agreement with the results from finite-element calculations. To obtain an accurate conversion of positions along the observation channel to times after mixing, which is required for the quantitative kinetic analysis of the measurements,¹⁵ we carried out time-resolved finite-element calculations (Figure S6 and Videos S1, S2).

We first demonstrate the performance of the microfluidic double-jump device for rapid processes on the millisecond time scale. To this end, we investigated the fast coupled folding and binding of the intrinsically disordered activation domain of the

Received: March 10, 2017

Published: April 10, 2017

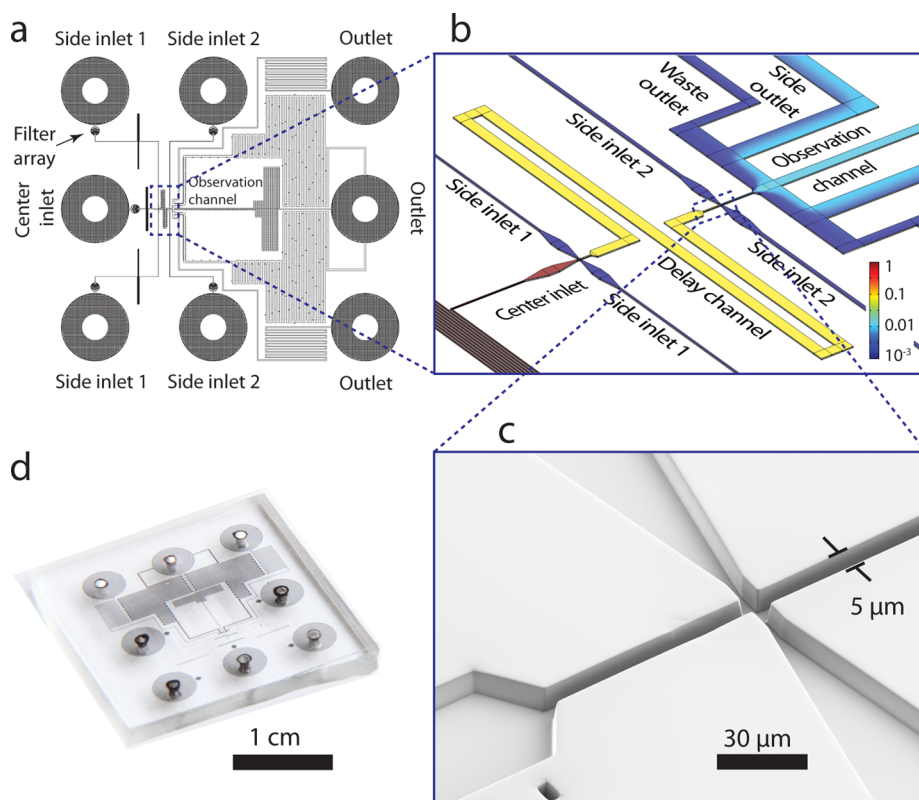


Figure 1. Design of the microfluidic double-jump mixing device. (a and b) Layout of the device: Solutes for the first mixing step are introduced from side inlets 1 (top and bottom) and mixed with the sample molecules from the center inlet. After passing a delay channel that defines the time between the two mixing steps, the sample is diluted by mixing with solutes from side inlets 2 (top and bottom). Microstructured filter arrays⁹ were incorporated after each inlet to prevent obstruction of the channels by traces of dust. The relaxation to equilibrium can be followed by measuring at different positions along the observation channel, as each position corresponds to a different time after mixing. To decelerate the flow rapidly and to have access to longer time scales (up to ~ 5 min) additional outlet channels perpendicular to the observation channel are included. A typical calculated concentration profile of sample molecules ($D = 10^{-10} \text{ m}^2/\text{s}$) introduced via the center inlet is shown in panel b. Relative concentrations are plotted on a logarithmic scale, with the initial relative sample concentration set to 1. Note that while the mixing of small solutes is completed after the first and second mixing steps, respectively (Figure S1), the sample molecules are not uniformly distributed after the second mixing step because of their smaller diffusion coefficient. The partitioning into waste and side outlets ensures that the sample concentration in the side outlets is high enough for data recording. (c) Scanning electron micrograph of the second mixing region in the PDMS device to illustrate the high quality of the structures. (d) Photograph of the microfluidic device. For visualization, the microchannels are filled with ink.

p160 transcriptional coactivator (ACTR) and the nuclear coactivator binding domain (NCBD) of CREB-binding protein,¹⁶ essential regulators of eukaryotic transcription.¹⁷ In the first mixing step, ACTR labeled with Cy3B and LD650¹⁸ as Förster resonance energy transfer (FRET) donor and acceptor, respectively, is delivered from the center inlet and mixed with an excess of unlabeled NCBD from the side inlets (100 nM initial concentration) to induce complex formation (Figure 2a). The following 5 mm-long channel serves as a delay line along which the two proteins have time to associate for 20 s. In the second mixing step, dissociation of the preformed complex is then triggered by dilution with buffer.

Figure 2b shows transfer efficiency histograms recorded after the first (left panel) and second mixing step (right panel), with the first histograms measured at 10 and 7 ms after mixing, respectively (Figures S7 and S8). To quantify the concentration dependence of this bimolecular reaction, the experiments were repeated with initial NCBD concentrations of 200 and 400 nM NCBD. A global kinetic analysis of all three data sets (Figure 2c) yields a dissociation rate coefficient of $7.1 \pm 0.4 \text{ s}^{-1}$ and an association rate coefficient of $0.6 \pm 0.2 \text{ nM}^{-1} \text{ s}^{-1}$ (see Materials and Methods and Figure S9 for details), in agreement with previous stopped-flow results.¹⁹ By fabricating devices with

different lengths of the delay channel, we can interrogate the effect of the association time on the dissociation kinetics. In the present case, reducing the association time to 25 ms (corresponding to a 87- μm delay channel) yields an identical dissociation rate coefficient (Figure S10), indicating the absence of long-lived kinetic intermediates during complex formation.

To illustrate the suitability of the device for resolving more complex conformational changes in biomolecules over a broad range of time scales, we investigate a recently identified transient intermediate in the conformational transition of the pore-forming toxin ClyA.²⁰ ClyA is expressed as a soluble monomer that, upon interaction with membranes or detergent, undergoes a large conformational rearrangement into its protomer conformation.²¹ This monomer-to-protomer transition involves a kinetic intermediate that is denatured and expanded.²⁰ However, owing to its transient nature, the properties of this intermediate have largely remained elusive. Here we use the microfluidic double-jump device to first form the intermediate state of ClyA by mixing the FRET-labeled protein with the membrane-mimicking detergent *n*-dodecyl- β -D-maltopyranoside (DDM) (Figure 3a); after 20 s in the delay channel, the low-FRET (i.e., rather expanded) intermediate is

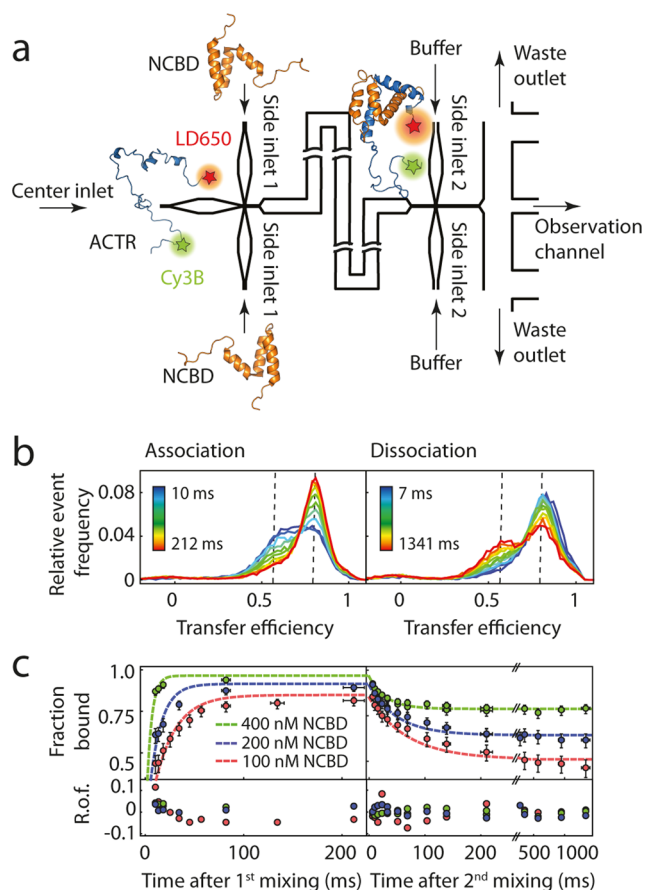


Figure 2. Coupled folding and binding of the intrinsically disordered proteins ACTR and NCBD investigated with the double-jump mixing device. (a) Donor- and acceptor-labeled ACTR is mixed in the first step with an excess of unlabeled NCBD to induce complex formation. Dissociation is triggered in the second mixing step by dilution with buffer solution. (b) Transfer efficiency histograms measured at various positions along the channels after the first and second mixing steps (left and right panel, respectively; normalized to an area of 1), corresponding to different times after the start of the reaction (as indicated by the color scale). The low transfer efficiency peak, $\langle E \rangle \approx 0.60$, corresponds to free ACTR and the high transfer efficiency peak, $\langle E \rangle \approx 0.80$, to folded ACTR within the complex with NCBD (100 nM initial concentration). (c) Global fit (dashed colored lines) of the association (left) and dissociation kinetics (right) for three different initial NCBD concentrations (100, 200, and 400 nM). The error bars indicate the uncertainties from fitting the transfer efficiency histograms, and the bottom panels depict the residuals of the fit (R.o.f.).

maximally populated. In the second mixing step, the protein is stripped of detergent by rapid mixing with β -cyclodextrin, a cyclic oligosaccharide that efficiently sequesters detergent molecules²² (Figure S11). The second jump enables us to return to the initial solution conditions and investigate whether and how the intermediate of ClyA returns to the initial monomeric conformation.

Within the dead time of the measurement after the second mixing step, a broad transfer efficiency distribution with an average of $\langle E \rangle \approx 0.61$ is formed (Figure 3b), corresponding to a rapid collapse of the polypeptide chain. The pronounced broadening beyond the shot noise width is indicative of slow dynamics within the resulting conformational distribution.^{5,23,24} Only on a much longer time scale of 5 ± 1 s, a transition takes place to a population with a transfer efficiency of ~ 0.43 ,

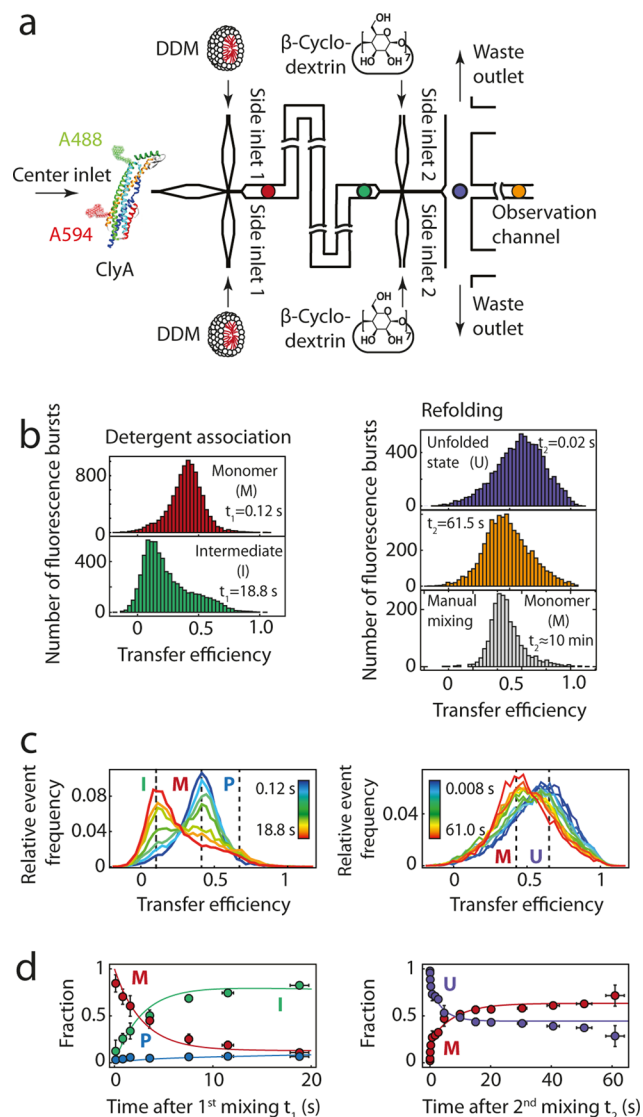


Figure 3. Probing the intermediate state of the pore-forming toxin ClyA by rapid double-jump mixing. (a) Schematic of the measurement. (b) Transfer efficiency histograms measured at different positions in the device (indicated by corresponding colored circles in panel a) reveal different ClyA conformations. Mixing of ClyA in its monomer conformation (M) with *n*-dodecyl β -D-maltopyranoside (DDM, 0.11% w/v) induces the formation of a denatured intermediate state (I). After I is maximally populated in the delay channel, the protein is stripped of detergent by addition of the cyclic oligosaccharide β -cyclodextrin (0.058% w/v) in the second mixing step, which causes a collapse of I to the compact unfolded state U. Within ~ 1 min, ClyA returns to the average transfer efficiency of M. In manual mixing experiments (lowest panel on the right), complete conversion to the narrow transfer efficiency distribution of the monomer is observed. (c) Normalized transfer efficiency histogram time series indicating the time-course of the transition from M ($\langle E \rangle = 0.42$) to I ($\langle E \rangle = 0.13$) after the first mixing step (left), and from U ($\langle E \rangle = 0.61$) to M ($\langle E \rangle = 0.43$) after the second mixing step (right). The transition from I to U occurs within the dead time (7 ms). (d) Left panel: Fractions of monomer (M), intermediate (I) and protomer (P) after the first mixing step obtained from a global fit of the histograms (colored circles), overlaid with a kinetic off-pathway model using previously described rates²⁰ (lines). Right panel: Fractions of M and U after the second mixing step fitted with a biexponential fit (for M: $\tau_1 = 0.2 \pm 0.1$ s, 36% of total amplitude, and $\tau_2 = 8.0 \pm 1.9$ s, 64% of total amplitude) (see Materials and Methods for details).

characteristic of the known folded monomer conformation²⁰ (Figure 3c,d, Figures S12, S13 and Table S1). Further narrowing of the transfer efficiency distribution is observed by measurements in the additional observation channel up to 4.5 min after mixing (Figure S14). Full conversion to the narrow histogram of the monomer, however, is only complete after ~10 min, as revealed by manual mixing experiments (Figure 3b), which can be combined with the longest time scales accessible in the mixer without any time gap. Overall, the results on ClyA illustrate the capacity of double-jump mixing to probe the behavior of complex kinetics and intermediates that would otherwise be inaccessible.

In summary, we present here a microfluidic device for rapid double-jump mixing experiments in combination with single-molecule spectroscopy, with observation times from milliseconds to minutes after mixing. The approach combines the advantages of nonequilibrium perturbation techniques with the ability of single-molecule spectroscopy to resolve conformational heterogeneity. The technique is particularly valuable for probing transiently populated states that are neither accessible at equilibrium nor in single-step mixing experiments. The device thus enables the discovery of elusive transient species in biomolecular mechanisms and provides a powerful extension of the single-molecule toolbox.

■ ASSOCIATED CONTENT

Supporting Information

The Supporting Information is available free of charge on the ACS Publications website at DOI: 10.1021/jacs.7b02357.

Materials and methods section and additional figures (PDF)

Video of the time-resolved finite element calculation (AVI)

Video of the time-resolved finite element calculation (AVI)

Copy of the design file for the photomask (ZIP)

■ AUTHOR INFORMATION

Corresponding Author

*schuler@bioc.uzh.ch

ORCID

Benjamin Schuler: 0000-0002-5970-4251

Notes

The authors declare no competing financial interest.

■ ACKNOWLEDGMENTS

We thank Scott Blanchard for the generous gift of LD650 maleimide. We thank Donat Scheiwiler, Stefan Blunier (Institute of Mechanical Systems, ETH Zurich), and Vincent Romain Joseph Martinez for help with microfabrication; the Center for Microscopy and Image Analysis (University of Zurich) for assistance and support with scanning electron microscopy; Adrian Schmid and Sascha Weidner for technical assistance; Hagen Hofmann and Karin Buholzer for providing an expression plasmid for ACTR and NCBD; Jendrik Schöppe and Andreas Plückthun for providing the pAT222-pD vector, and Ruth Kellner for the photographs of the microfluidic device. This work was supported by the Swiss National Science Foundation (B.S.) and by a postdoctoral fellowship from the Forschungskredit of the University of Zurich (N.Z.).

■ REFERENCES

- (1) Selvin, P. R.; Ha, T. *Single-molecule techniques: A laboratory manual*; Cold Spring Harbor Laboratory Press: New York, 2008.
- (2) Schuler, B.; Hofmann, H. *Curr. Opin. Struct. Biol.* **2013**, *23*, 36.
- (3) Holmstrom, E. D.; Nesbitt, D. J. *Annu. Rev. Phys. Chem.* **2016**, *67*, 441.
- (4) Rigler, R.; Elson, E. S. *Fluorescence correlation spectroscopy: Theory and applications*; Springer: Berlin, 2001.
- (5) Gopich, I. V.; Szabo, A. Theory of single-molecule FRET efficiency histograms. In *Single-molecule biophysics: Experiment and theory*; Komatsuzaki, T.; Kawakami, M.; Takahashi, S.; Yang, H.; Silbey, R. J., Eds.; Advances in Chemical Physics; Wiley: Hoboken, NJ, 2012; Vol. 146; p 245.
- (6) Lipman, E. A.; Schuler, B.; Bakajin, O.; Eaton, W. A. *Science* **2003**, *301*, 1233.
- (7) Pfeil, S. H.; Wickersham, C. E.; Hoffmann, A.; Lipman, E. A. *Rev. Sci. Instrum.* **2009**, *80*, 055105.
- (8) Gambin, Y.; VanDelinder, V.; Ferreol, A. C. M.; Lemke, E. A.; Groisman, A.; Deniz, A. A. *Nat. Methods* **2011**, *8*, 239.
- (9) Wunderlich, B.; Nettels, D.; Benke, S.; Clark, J.; Weidner, S.; Hofmann, H.; Pfeil, S. H.; Schuler, B. *Nat. Protoc.* **2013**, *8*, 1459.
- (10) Welker, E.; Maki, K.; Shastry, M. C. R.; Juminaga, D.; Bhat, R.; Scheraga, H. A.; Roder, H. *Proc. Natl. Acad. Sci. U. S. A.* **2004**, *101*, 17681.
- (11) Krantz, B. A.; Sosnick, T. R. *Biochemistry* **2000**, *39*, 11696.
- (12) Knight, J. B.; Vishwanath, A.; Brody, J. P.; Austin, R. H. *Phys. Rev. Lett.* **1998**, *80*, 3863.
- (13) Gambin, Y.; Simonnet, C.; VanDelinder, V.; Deniz, A.; Groisman, A. *Lab Chip* **2010**, *10*, 598.
- (14) Duffy, D. C.; McDonald, J. C.; Schueller, O. J. A.; Whitesides, G. M. *Anal. Chem.* **1998**, *70*, 4974.
- (15) Wunderlich, B.; Nettels, D.; Schuler, B. *Lab Chip* **2014**, *14*, 219.
- (16) Dogan, J.; Schmidt, T.; Mu, X.; Engström, Å.; Jemth, P. *J. Biol. Chem.* **2012**, *287*, 34316.
- (17) Dyson, H. J.; Wright, P. E. *J. Biol. Chem.* **2016**, *291*, 6714.
- (18) Altman, R. B.; Terry, D. S.; Zhou, Z.; Zheng, Q.; Geggier, P.; Kolster, R. A.; Zhao, Y.; Javitch, J. A.; Warren, J. D.; Blanchard, S. C. *Nat. Methods* **2012**, *9*, 68.
- (19) Dogan, J.; Jonasson, J.; Andersson, E.; Jemth, P. *Biochemistry* **2015**, *54*, 4741.
- (20) Benke, S.; Roderer, D.; Wunderlich, B.; Nettels, D.; Glockshuber, R.; Schuler, B. *Nat. Commun.* **2015**, *6*, 6198.
- (21) Mueller, M.; Grauschopf, U.; Maier, T.; Glockshuber, R.; Ban, N. *Nature* **2009**, *459*, 726.
- (22) Otzen, D. E.; Oliveberg, M. *J. Mol. Biol.* **2001**, *313*, 479.
- (23) Kalinin, S.; Valeri, A.; Antonik, M.; Felekyan, S.; Seidel, C. A. J. *Phys. Chem. B* **2010**, *114*, 7983.
- (24) Nir, E.; Michalet, X.; Hamadani, K. M.; Laurence, T. A.; Neuhauser, D.; Kovchegov, Y.; Weiss, S. *J. Phys. Chem. B* **2006**, *110*, 22103.

Supporting Information

Rapid microfluidic double-jump mixing device for single-molecule spectroscopy

Fabian Dingfelder, Bengt Wunderlich, Stephan Benke, Franziska Zosel, Niels Zijlstra, Daniel Nettels & Benjamin Schuler*

Materials and Methods

Device design and stationary 3D finite-element calculations. Crucial design criteria were dilutions of $\sim 1:10$ and $\sim 1:20$ after the first and second mixing step, respectively. The greater dilutions after the second mixing step allow us to jump back to near-native conditions after populating transient states in the first mixing step. Additionally, we aimed for moderate flow velocities in the observation channel (~ 1 mm/s) that are compatible with single molecule detection, and for dead times in the low millisecond range. The lengths of the mixing necks were chosen such that mixing of solutes such as guanidinium chloride, salt, or small ligands from the side inlets ($D \approx 10^{-9}$ m²/s) is $>90\%$ complete (Figure S1). The layout of the device was optimized based on finite-element calculations carried out with COMSOL Multiphysics 4.3. The *Creeping Flow* module was utilized to calculate stationary flow velocities. Stationary concentrations were computed applying the *Transport of Diluted Species* module. Since the channel geometry is symmetric in height, only one half of the channels was modeled. The size of the rectangular mesh elements was optimized throughout the structure such that the regions with the largest gradients contained the finest mesh. For the calculation of the flow velocity, the mesh element size ranged from 500 nm in the mixing region to 100 μ m in the observation channel. For the concentration calculations, the mesh-resolution was increased to a range between 250 nm in the mixing region and 100 μ m in the observation channel. The translational diffusion coefficient of the sample provided from the center inlet was set to 10^{-10} m²/s (corresponding to a small protein), and the diffusion coefficient of the solute from side inlets 1 was set to 10^{-9} m²/s (corresponding to a small molecule such as denaturant, salt, or a small ligand) (Figure 1b and Figure S1). The channel geometry and inlet pressures were optimized such that the average flow velocity in the observation channel after the second mixing step was 1 mm/s and dilutions of 1:10 and $\sim 1:20$ after the first and second mixing step were obtained, respectively.

Time-resolved 3D finite-element calculations (position-to-time conversion). The 3D time-resolved finite-element calculations were performed as described previously¹. In brief, a Gaussian-shaped pulse in time (standard deviation 0.1 ms) that is spatially homogenous across the inlet boundary propagates along the channels of the device. Two sets of time-resolved calculations were carried out, corresponding to the two applications of the microfluidic device discussed in the main text. For the

first application (interaction of ACTR and NCBD), the translational diffusion coefficient was set to $10^{-10} \text{ m}^2/\text{s}$, and the calculations after the first mixing step were carried out in two steps (0 - 12.5 ms and 12.5 - 350 ms), with a mesh resolution of 100 nm in the mixing region. Calculations up to 350 ms were sufficient, as for all experimental conditions the equilibrium was established before that time. For time-resolved calculations after the second mixing step, calculations were also performed in segments (0 - 5 ms, 5 - 25 ms, 25 - 250 ms, 250 ms - 1.5 s and 1.5 s - 5 s), with a minimal element size of 66.7 nm (Figure S6 and Video S1-S2). To obtain the position-to-time conversion for the second application (conformational changes of ClyA), the experimentally determined translational diffusion coefficient ($6.8 \cdot 10^{-11} \text{ m}^2/\text{s}$) of ClyA² was used, and calculations after the first mixing step were carried out for four intervals along the delay channel (0 - 5 ms, 5 - 200 ms, 200 ms - 2s and 2 - 20 s). The calculations after the second mixing step were performed for the same intervals described for ACTR/NCBD, with an additional interval between 5 and 65 s. Because of Taylor dispersion³, sample molecules originating from different times after passing the mixing region contribute to the signal observed at a given position of the confocal volume along the observation channel. Thus, a concentration-weighted mean arrival time was calculated from the time-resolved concentration profiles obtained along the central streamline of the device¹:

$$\langle t \rangle(x) = \frac{\int t c(x,t) dt}{\int c(x,t) dt},$$

with $c(x,t)$ being the sample concentration as function of position, x , and time, t .

Fabrication of the silicon master for replica molding. The microfabrication of the silicon wafer used as a mold for producing poly(dimethylsiloxane) (PDMS) replicas was carried out essentially as described previously⁴. A 4-inch silicon wafer was exposed to hexamethyldisilazane (HMDS) for 30 s to promote adhesion of the photoresist. Subsequently, 3 mL of negative photoresist (ma-N 1410, micro resist technology GmbH) were spin-coated on the wafer, resulting in a $\sim 1 \mu\text{m}$ -thick layer. Then, the wafer was soft-baked on a hot plate: starting at room temperature, the wafer was baked for 90 s once 395 K were reached. Utilizing a mask aligner (MA6/MB6, Süss), a chrome mask (Compugraphics Jena) was aligned 20 μm on top of the wafer and exposed to UV light (energy density: 450 mJ/cm^2 at 365 nm). Non-crosslinked photoresist was removed by gently shaking the wafer in resist developer (ma-D533/S, micro resist technology GmbH) for ~ 10 s. After completion of the photolithography, the wafer was transferred to a silicon etch system (Estrelas 100, Oxford Instruments). Using deep reactive-ion etching, the microstructures were etched 10 μm deep in a 3-step Bosch process. Residual photoresist was removed by placing the wafer in a plasma processor (300 E, TePla) for 5 min. The etching depth was verified with a white-light interferometer (NewView 5000, Zygo).

Replica molding, assembly, and application of the microfluidic device. Replica molding and the chip-to-world connection of the microfluidic device was carried out as described by Wunderlich *et al.*⁴. In brief, the two components, A (silicone rubber compound) and B (curing agent), of a PDMS kit (RTV 615 A+B, Momentive Performance Materials) were mixed in a 10:1 ratio, stirred thoroughly, and degassed in a desiccator to eliminate bubbles. The silicon wafer was exposed to trichloromethylsilane for ~ 30 min to prevent adhesion of PDMS to the wafer and was then transferred to a casting dish. After

filling it with degassed PDMS, the casting dish was transferred to an oven and the PDMS cured overnight at 333 K. The replica was removed, and 1.5-mm holes were punched into the inlets and outlets of the PDMS devices (Harris Uni Core 15075 cutting tips). The device was then bonded to a clean 25 mm x 25 mm fused-silica cover slide (Esco Optics) after plasma activation (FEMTO, Diener). To prevent contamination, the assembly of the microfluidic device was carried out in a laminar-flow bench. The device was mounted in a custom-built cartridge and loaded in a holder^{2, 4}. A tight seal of the PDMS to the cartridge was ensured by applying vacuum to one of the cartridge inlets. Flow of solutions through the microchannels was driven by applying pressurized air to the center and side inlets and by applying negative pressure to the outlets via polyurethane tubing. The pressures were regulated by electropneumatic pressure transducers (Type 3110, Marsh Bellofram) connected to National Instruments data acquisition cards (NI 9201 and NI 9264). A custom-written LabVIEW (National Instruments) program allowed the pressures to be set, read off, and recorded. Before each microfluidic mixing measurement, the pressures were additionally confirmed using a digital manometer.

Scanning electron microscopy. Scanning electron microscopy (SEM) of the microfluidic devices was carried out on a Zeiss SUPRA 50 VP microscope at the Center for Microscopy and Image Analysis (University of Zurich). The PDMS devices were sputtered with a 5-10 nm layer of platinum in a high-vacuum coating unit (CCU-010, Safematic). SEM micrographs were used to quantify the dimensions of the microfluidic channels and to assess the quality of the microstructures (Figure 1c and Figure S2).

Widefield fluorescence imaging. Widefield fluorescence imaging was performed on an inverted microscope equipped with a 488 nm solid state laser (Sapphire 488-100, Coherent). The laser light (~8 mW) was focused onto the back aperture of a microscope objective (Plan, 20x/0.40, Olympus) via a dichroic mirror (488 nm, Semrock). After passing an emission bandpass filter (Brightline HQ525/50, Chroma), the fluorescence emission was imaged onto an EM-CCD camera (Ixon 87 BI, Andor). The center inlet and side inlets 1 of the device were filled with 5 μ M of 20 kDa FITC-labeled Dextran (FD20S, Sigma Aldrich) and diluted with 50 mM sodium phosphate buffer, pH 7, from the side inlets 2. The pressures applied were 8.89 kPa (1.29 psi) to the center inlet, 8.69 kPa (1.26 psi) to the side inlets 1, 10.96 kPa (1.59 psi) to the side inlets 2, and -13.79 kPa (-2 psi) to the outlets (Figure S3).

Fluorescence correlation spectroscopy (FCS). Sample dilutions after the first and second mixing step of the microfluidic device were quantified with FCS measurements on a custom-built confocal instrument. Excitation light at 532 nm from a continuous-wave solid-state laser (Laser Boxx, Oxxius) was coupled into the microscope objective (UplanApo 60/1.20W, Olympus) via a triple-band dichroic mirror (z488/532/633, Chroma) at a power of 50 μ W. Fluorescence was collected via the same objective, focused onto a 100 μ m pinhole, separated with a polarizing beam splitter and two dichroic mirrors (585DCXR, Chroma), additionally filtered by bandpass filters for the donor channels (ET525/50, Chroma) and for the acceptor channels (HQ650/100 Chroma), and then focused onto four single-photon avalanche detectors (SPCM-AQR-13, Perkin Elmer and τ -SPAD, PicoQuant). Photon arrival times were recorded by four channels of a HydraHarp 400 counting module (PicoQuant). Measurements were carried out in 50 mM sodium phosphate buffer containing 0.01% (w/v) Tween 20

(pH 7.0). The initial concentration of sample molecules (ACTR doubly labeled with Cy3B and LD650) was 5 nM. To quantify the sample dilution after the first mixing step, side inlets 1 and 2 were filled with buffer. The laser focus was positioned in the center inlet as well as at the end of the delay channel ($x = 5$ mm) and the fluorescence signal was recorded for 15 minutes. For the determination of sample dilution after the second mixing step, the solutions in the side inlets 1 were replaced by doubly labeled ACTR, and 7 min. measurements were carried out at the end of the delay channel and in the observation channel ($x = 4$ mm, with x being the distance from the center of the second mixing region). The pressures applied were 8.89 kPa (1.29 psi) to the center inlet, 8.69 kPa (1.26 psi) to the side inlets 1, 10.96 kPa (1.59 psi) to the side inlets 2, and -13.79 kPa (-2 psi) to the outlets. The fluorescence intensity donor-acceptor cross-correlation curves were fitted with the model for laminar flow and diffusion by Magde *et al.*⁵:

$$G(\tau) = 1 + \frac{1}{N} \left[\left(1 + \frac{\tau}{\tau_D} \right) \sqrt{1 + s^2 \frac{\tau}{\tau_D}} \right]^{-1} \exp \left[- \left(\frac{\tau}{\tau_{Drift}} \right)^2 \frac{1}{(1 + \tau / \tau_D)} \right],$$

where N is the average number of doubly labeled particles in the confocal volume, and τ_D is the translational diffusion time, which is constrained to the value measured in the absence of flow in a separate measurement. s is the aspect ratio of the confocal volume, which is assumed to be of Gaussian shape. τ_{Drift} is the drift time, which can be related to the flow velocity, v , via $v = 2r / \tau_{Drift}$, where r is the lateral radius of the confocal volume (Figure S4).

Two-focus fluorescence correlation spectroscopy (2f-FCS). Flow velocities in the microfluidic device were determined by 2f-FCS of Alexa Fluor 488 as described previously^{1,6}. Briefly, 2f-FCS measurements were performed on a confocal single-molecule instrument (MT200, PicoQuant), where two foci with an interfocus distance of 400 nm (calibrated as previously described⁷) are generated using a differential interference contrast prism (U-DICTHC, Olympus) with the two foci being aligned in the direction of flow. Two orthogonally polarized, pulsed diode lasers at 485 nm (LDH-D-C-485; PicoQuant) with repetition rates of 20 MHz and laser powers of 30 μ W each were used to alternately excite the sample. Fluorescence emission, collected by the objective, was focused on a 150 μ m pinhole before being distributed by a 50/50 beam splitter on two single-photon avalanche photodiodes (τ -SPAD 50, PicoQuant) after passing a bandpass filter (ET525/50M, Chroma). The photon arrival times were recorded by two channels of a HydraHarp 400 counting module (PicoQuant). Fluorescence intensity auto- and cross-correlation curves from the data of each focus were globally fitted with the model of Arbour *et al.* (including a triplet component) to obtain flow velocities⁶. To determine the translational diffusion time independently, 0.7 nM Alexa Fluor 488 dissolved in doubly distilled water containing 0.001% Tween was measured in the absence of flow. For the flow velocity measurements in the microfluidic device, the same sample was loaded in both the center and the side inlets. Using a piezo stage combination (P-733.2 and PIFOC, PI) the laser foci were positioned inside the observation channel, and the fluorescence signal was recorded for two to three minutes at each position. The pressures applied were 8.89 kPa (1.29 psi) to the center inlet, 8.69 kPa (1.26 psi) to the side inlets 1, 10.96 kPa (1.59 psi) to the side inlets 2, and -13.79 kPa (-2 psi) to the outlets (Figure S5).

Protein expression, purification, and labeling. The coding sequence of a double-cysteine ACTR mutant was cloned via BamHI/HindIII into a pAT222-pD expression vector (gift of J. Schöppe and A. Plückthun)⁸, yielding an expression construct with an N-terminal Avi-tag and a Thrombin-cleavable C-terminal His₆ tag of the following sequence:

MAGLNDIFEAQKIEWHEGSMGSGSGPCGTQNRPLLNSLDDLVGPPSNLEGQSDERALDQLHTLLSNTDATGLE
EIDRALGIPELVNQGQALEPKQDCGGPRGSRSQASHHHHHH. pBirAcm (Avidity) was co-transfected *for in vivo* biotinylation of Lys12 in the Avi tag, and expression was carried out in *E.coli* BL21(DE3) as described before⁹. The harvested cells were lysed by sonication and the His-tagged protein was enriched via immobilized metal affinity chromatography (IMAC) on Ni-IDA resin (ABT). The His₆ tag was then cleaved off with thrombin (Serva Electrophoresis) and separated from the protein by another IMAC purification step. Finally, biotinylated protein was separated from impurities and non-biotinylated protein via reversed-phase HPLC on a C18 column (Reprosil Gold 200, Dr. Maisch) with a water/0.1%TFA-acetonitrile gradient. Purified protein was lyophilized.

For labeling with the FRET dye pair, ACTR was dissolved under nitrogen atmosphere to a concentration of 200 μ M in 100 mM potassium phosphate buffer, pH 7.0 (labeling buffer). The protein was then labeled for 3 h at room temperature with a 0.8-fold molar ratio of Cy3B maleimide (GE Healthcare) to protein. Labeled protein was separated from unlabeled protein with RP-HPLC on a Sunfire C18 column (Waters) as described above. The appropriate fraction was lyophilized, re-dissolved in labeling buffer, and labeled with a 0.8-fold molar ratio of LD650 maleimide¹⁰ (Lumidyne Technologies) to protein. Double-labeled protein was separated from free dye on a Reprosil Gold 200 column and subjected to RP-HPLC on a Sunfire C18 column as a final purification step. The correct mass of labeled ACTR was confirmed by electrospray ionization mass spectrometry.

NCBD was co-expressed with ACTR¹¹ from a pET-47b(+) vector. The expression construct contained an N-terminal His₆ tag cleavable with HRV 3C protease, yielding the final sequence:

MAHHHHHSAALEVLFQGPCPNRSISPSALQDLLRTLKSPSSPQQQQVLNILKSNPQLMAAFIKQRTAKYVANQ
PGMQ. Cell lysis and protein enrichment via IMAC were carried out as described for ACTR, followed by enzymatic cleavage of the His₆ tag with HRV 3C protease and separation of the tag from the protein via another round of IMAC. Finally, ACTR and NCBD were separated with RP-HPLC as described above.

ClyA was expressed, purified, and labeled as described previously².

Passivation of microfluidic devices. To reduce surface adhesion of the sample proteins to the channel walls, the microchannels were passivated prior to single-molecule measurements. For the ACTR/NCBD experiments, passivation was achieved by flushing all channels of the device with an aqueous solution of 0.1 mg/ml poly(L-lysine)-*graft*-poly(ethylene glycol) (PLL/PEG) (PLL(20)-g[3.5]-PEG(2), Susos) for at least 1 hour, and subsequent flushing with buffer solution 1 (50 mM sodium phosphate, 1 mM β -mercaptoethanol, 0.01% (w/v) Tween 20, pH 7.0) for at least 20 min. For the measurements with ClyA, the channels were pretreated with a mixture of bovine serum albumin (BSA) and PLL/PEG (0.1 mg/mL) for at least 1 hour, followed by flushing with buffer solution 2 (25 mM sodium phosphate, 75 mM sodium chloride, 140 mM β -mercaptoethanol, 0.001% (w/v) Tween 20, pH 7.0). Intensity scans of the channel cross sections after passivation indicate the absence of progressive loss of sample molecules along the delay- and observation channel due to nonspecific surface interactions (Figure S15).

Single-molecule FRET measurements. Single-molecule FRET measurements of ACTR/NCBD were performed at 295 K on a custom-built instrument (for details see section *Fluorescence correlation spectroscopy (FCS)*) with excitation light at 532 nm from a continuous-wave laser (Laser Boxx, Oxxius, France) at an excitation power of 50 μ W. Measurements were carried out in buffer solution 1. For determining the affinity of ACTR towards NCBD, increasing concentrations of NCBD were titrated to 100 μ M of doubly-labeled ACTR (Figure S9a). Measurements were conducted in custom-made quartz cuvettes that were plasma-cleaned and pretreated for half an hour with 0.1 mg/ml PLL/PEG to minimize protein-surface interactions. For the microfluidic measurements, fluorescently labeled ACTR (4-6 nM) was supplied from the center inlet and mixed with 100, 200, or 400 nM of unlabeled NCBD, respectively, from side inlets 1. The buffer inlets 2, which supply the solutions for the second mixing step, were filled with buffer solution 1, and the pressures applied were 15.79 kPa (2.29 psi) to the center inlet, 15.58 kPa (2.26 psi) to the side inlets 1, 17.86 kPa (2.59 psi) to the side inlets 2, and -13.79 kPa (-2 psi) to the outlets (Figure 2b and Figures S7-S8). Note that in order to better resolve the millisecond association and dissociation kinetics of the ACTR/NCBD complex, slightly higher pressures were applied, yielding an average flow velocity in the observation channel of 1.25 mm/s.

Measurements of ClyA were performed at 295 K using a confocal single-molecule instrument (MT200, PicoQuant). To remove the contribution of molecules with inactive acceptor, pulsed interleaved excitation (PIE) was used¹². The donor dye was excited with a pulsed diode laser (LDH -D-C-485, PicoQuant) with a repetition rate of 20 MHz at an excitation power of 100 μ W. The acceptor dye was excited using a pulsed supercontinuum white-light laser (Fianium, PicoQuant) operating at 20 MHz and an excitation power of 35 μ W after passing a z582/15 band-pass filter (Chroma). The laser light was focused and epifluorescence collected via an UplanApo 60/1.20W objective (Olympus). The fluorescence light passed a chromatic beam splitter (R405/488/594, Chroma) and a 100 μ m pinhole and is split first by polarization (polarization cube, PicoQuant) and then by color (595 DCXR, Chroma). Before detection by four avalanche photodiodes (τ -SPAD, PicoQuant), emitted photons were filtered by E525/50M or HQ650/100 band-pass filters for donor and acceptor channels, respectively. Photon arrival times were recorded by a HydraHarp 400 counting module (PicoQuant) with 16-ps time resolution. The center inlet of the microfluidic device was filled with 20 μ L of 15 nM fluorescently labeled ClyA in buffer solution 2. Side inlets 1 supplied a 0.11% (w/v) solution of DDM for the first mixing step. Side inlets 2 were filled with 0.058% (w/v) β -cyclodextrin (Sigma-Aldrich). The pressures applied were 8.89 kPa (1.29 psi) to the center inlet, 8.69 kPa (1.26 psi) to the side inlets 1, 10.96 kPa (1.59 psi) to the side inlets 2, and -13.79 kPa (-2 psi) to the outlets (Figure 3b-c and Figures S12-S14).

Single-molecule FRET data analysis. For PIE measurements, only photons after donor excitation were used for the construction of transfer efficiency histograms. Emission after donor excitation was corrected for the different quantum yields of the dyes, the different detection efficiencies of the detectors, cross-talk, acceptor direct excitation, and background. For PIE measurements, only bursts that showed emission after direct acceptor excitation were selected, with a stoichiometry ratio (S) of less than 0.7, where S is defined as $S = n_{Dex}/(n_{Dex} + \gamma n_{Aex})$, with n_{Dex} being the total number of photons after donor excitation, n_{Aex} the total number of photons after direct acceptor excitation; γ is a correction factor chosen such that the main FRET population is located at $S = 0.5$. Bursts exhibiting acceptor photobleaching were excluded from further analysis¹³. The resulting bursts were binned in a histogram according to their transfer efficiency (E), calculated for each selected burst from the number

of photons from the corrected donor (n_D) and acceptor photon counts (n_A) after donor excitation according to $E = n_A/(n_A + n_D)$.

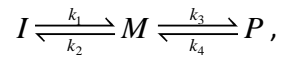
For the evaluation of the microfluidic mixing data with ACTR/NCBD, consecutive photons with interphoton times of less than 50 μs were combined into one fluorescence burst. The flow velocity after the first mixing step is fourfold lower than after the second mixing step, resulting in longer residence times in the confocal volume and thus larger bursts in the first step. Correspondingly, a higher burst identification threshold was applied for the first mixing step (70 photons per burst) compared to the second mixing step (40 photons per burst). All transfer efficiency histograms recorded after the first and second mixing step were fitted globally with a two-population model, with both populations being described by Gaussian peak functions. The positions and widths of the transfer-efficiency peaks were globally shared fit parameters, with the ratio of the peak widths being constrained to the value expected from shot-noise limited peak widths at the respective mean transfer efficiencies (Figures S7-S8). For each histogram, the fraction of bound ACTR, i.e., the fraction of complex (f_b), was determined from the fraction of the area of the high-efficiency peak. The uncertainty from the global fit was estimated by fixing the low transfer efficiency peak to a 15% broader and narrower Gaussian peak function, compared to the initial fit. The resulting fractions of bound ACTR as a function of time were then used as error margins. The errors on the arrival time originate from the estimated uncertainty in positioning the confocal volume along the observation channel (0.5 μm) and the uncertainty in flow velocity (5%)⁴. The datasets for the association and dissociation reaction at the three different NCBD concentrations (100, 200, and 400 nM NCBD) were fitted globally with a two-state model, assuming pseudo-first-order reaction conditions. The dissociation rate coefficient was a shared fit parameter, and the association rates, k_b , after the first and second mixing steps were free fit parameters (Figure 2c). Owing to residual surface adsorption of proteins in the microfluidic channels, the concentration of NCBD present in the observation channel cannot be determined accurately based on the concentration provided in the inlet channels. To determine the actual NCBD concentrations present during dissociation, we used the dissociation equilibrium constant, K_D , determined in an independent equilibrium experiment. From the asymptotic fit values of the global fit (Figure 2c), yielding the fraction of bound ACTR at equilibrium after completion of the dissociation reaction, and the K_D , the actual NCBD concentration was calculated as

$$c_{NCBD} = K_D \frac{f_b}{1 - f_b}.$$

The resulting NCBD concentrations were plotted against the observed association rates, and from the slope of a linear fit, the association rate coefficient for NCBD binding to ACTR was determined (Figure S9c). Note that we do not include the association rates after the first mixing step into this linear fit, since the NCBD concentration in the delay channel cannot be determined accurately (because the fraction of bound ACTR is not a sensitive measure for the NCBD concentration at bound fractions >0.9).

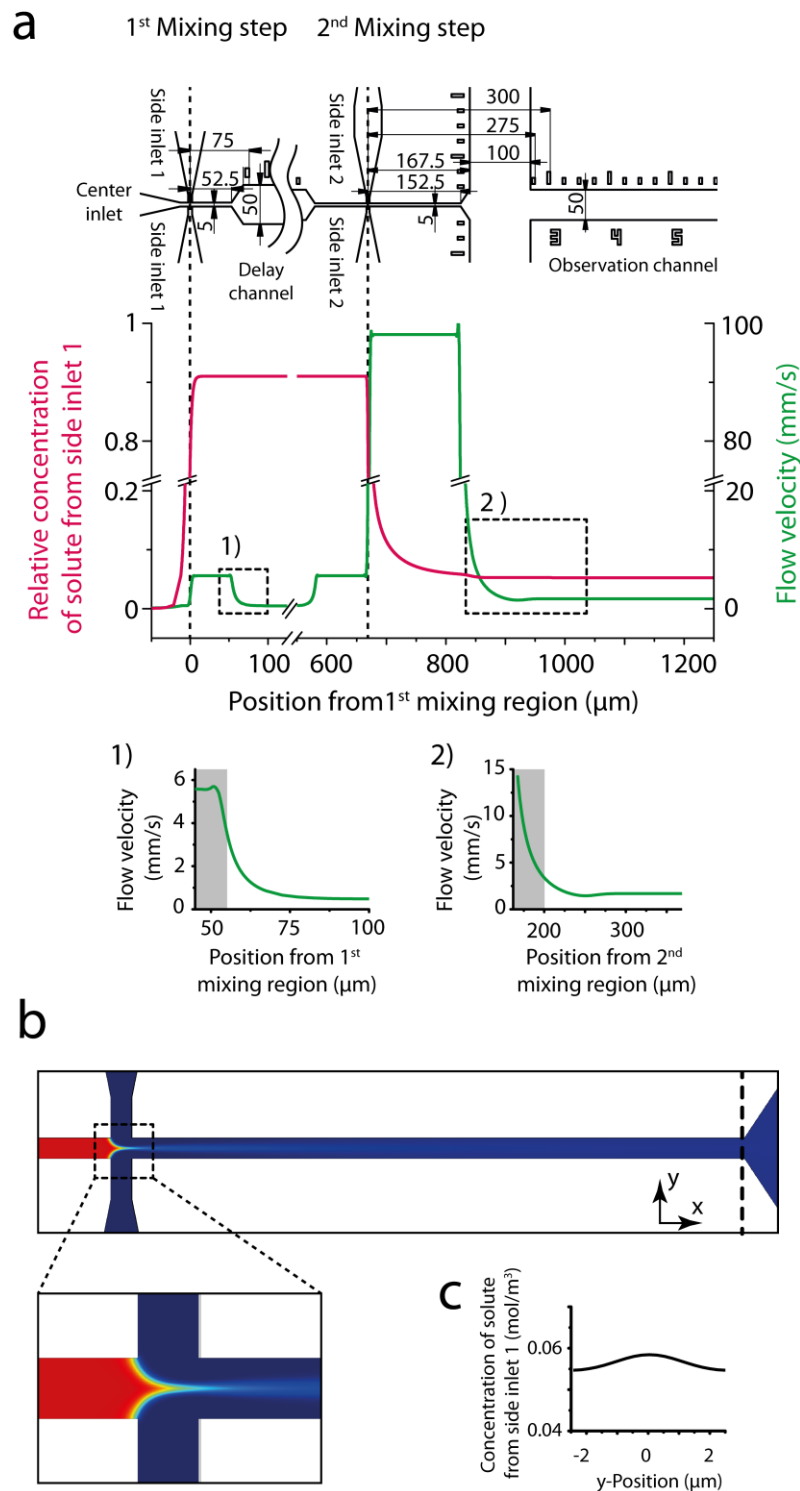
For the identification of fluorescence bursts in measurements with ClyA, contiguous photons with interphoton times of less than 150 μs after donor excitation were combined into one burst. For measurements after the first mixing step, bursts containing more than 70 photons per burst were considered for data analysis. After the second mixing step, a threshold of 25 photons per burst was applied (Figure 3b-c and Figures S12-S14). The transfer efficiency histograms recorded after the first mixing step were globally fitted with a log-normal peak function for the asymmetric peak of the intermediate and two Gaussian peak functions for the symmetric peaks of monomer and protomer,

using the widths and positions of all populations as shared parameters for all histograms of the time series. Since the protomer is only marginally populated, its peak width was constrained to 0.098, the value obtained in previous microfluidic measurements². The fractions obtained from the peak areas, with the error referring to the standard deviation of two independent measurements, were overlaid with a kinetic off-pathway model using previously described rate coefficients²:



with $k_1=0.3 \text{ s}^{-1}$, $k_2=0.05 \text{ s}^{-1}$, $k_3=0.02 \text{ s}^{-1}$ and $k_4=0.0005 \text{ s}^{-1}$ (Figure 3d, left panel). Transfer efficiency histograms after the second mixing step were approximated with two Gaussian peak functions (unfolded and native state). For the global fit, the position and width of the peak representing the unfolded state were constrained to the values obtained from fitting the transfer efficiency histogram recorded at the earliest time after mixing. Position and width of the second peak were globally shared fit parameters (Figure 3d right panel). The native fractions obtained from the peak areas as a function of time were fitted with a double-exponential fit. The errors of the time constants correspond to the standard errors of the fit. Error bars for the arrival times arise from the estimated uncertainty in positioning the laser focus along the observation channel and the variation in flow velocity⁴.

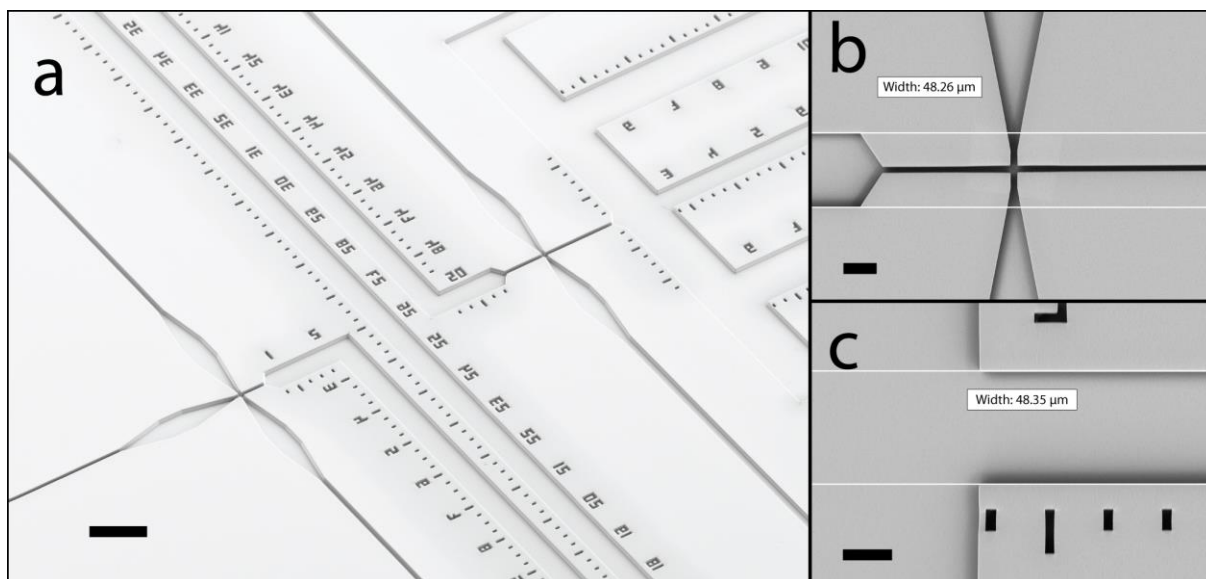
Figure S1. Flow velocities and concentrations in the microfluidic device from 3D finite-element calculations.



Important design considerations for the microfluidic double-jump mixing device are moderate flow velocities in the delay- and observation channel to be able to collect a sufficiently large number of photons while the sample molecules pass through the confocal detection volume. Additionally, we aim for dilutions that are sufficient for achieving large changes in intermediate populations. (a) Flow velocity (green) and concentration of the solute from side inlet 1 (red) along the central streamline of

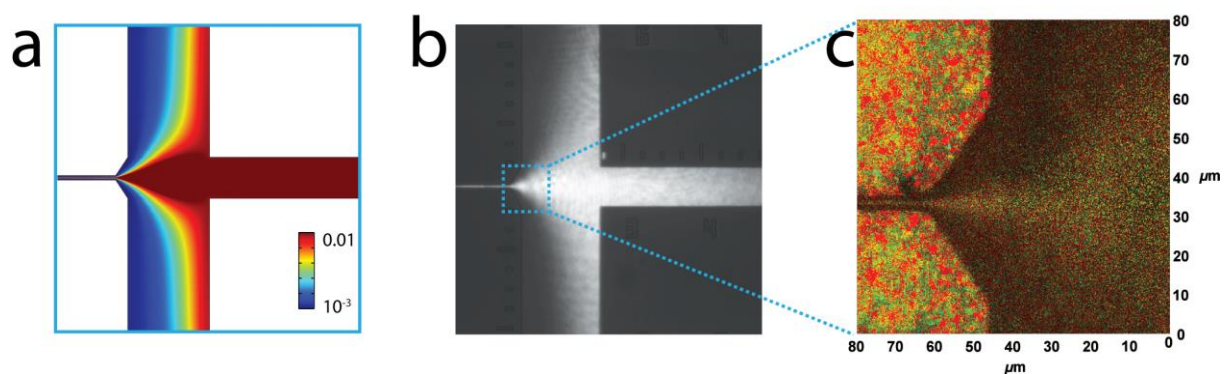
the device. Depicted on top are the channel dimensions of the two mixing regions (in micrometers). In the first mixing step, a 1:10 mixing ratio of solutions from the center inlet and the side inlets results in an increase in the relative concentration of the solute from side inlets 1 from 0 to 0.91. In the second mixing step, this concentration decreases to 0.053, corresponding to a 17-fold dilution. The device is designed for mixing a small protein ($D \approx 10^{-10} \text{ m}^2/\text{s}$) from the center inlet with small solutes ($D \approx 10^{-9} \text{ m}^2/\text{s}$), such as guanidinium chloride, from side inlets 1 and 2, for which mixing is complete by the end of the first mixing channel (see b and c). Of course, mixing with slower-diffusing species from side inlet 1 and/or 2 (e.g. another protein) is also feasible. Note that in this case the dilution factor of the second mixing step can depend on the diffusion coefficient of the solute in side inlets 1 and 2, since the fraction of molecules reaching the additional observation channels increases with increasing diffusion coefficient. Also shown in 1) and 2) is the decrease in flow velocity after passing the narrow mixing necks (ranges indicated as dashed boxes above). The shaded regions indicate the positions following the mixing regions that are inaccessible for measurements because the residence times of single sample molecules in the confocal volume are too short for a sufficient number of photons to be observed per burst. (b) Results of finite-element calculations, demonstrating that mixing of solutes from side inlet 1 is complete to more than 90 % at the end of the second mixing neck. (c) Concentration profile of the solute provided from side inlet 1 at the end of the mixing neck (position indicated by the black dashed line in (b)). Note that larger molecules (e.g. proteins) arriving from the center inlet are not uniformly distributed across the channel at the end of the mixing neck owing to their lower diffusion coefficient (see Figure 1).

Figure S2. Quality of microfabrication assessed by scanning electron microscopy (SEM).



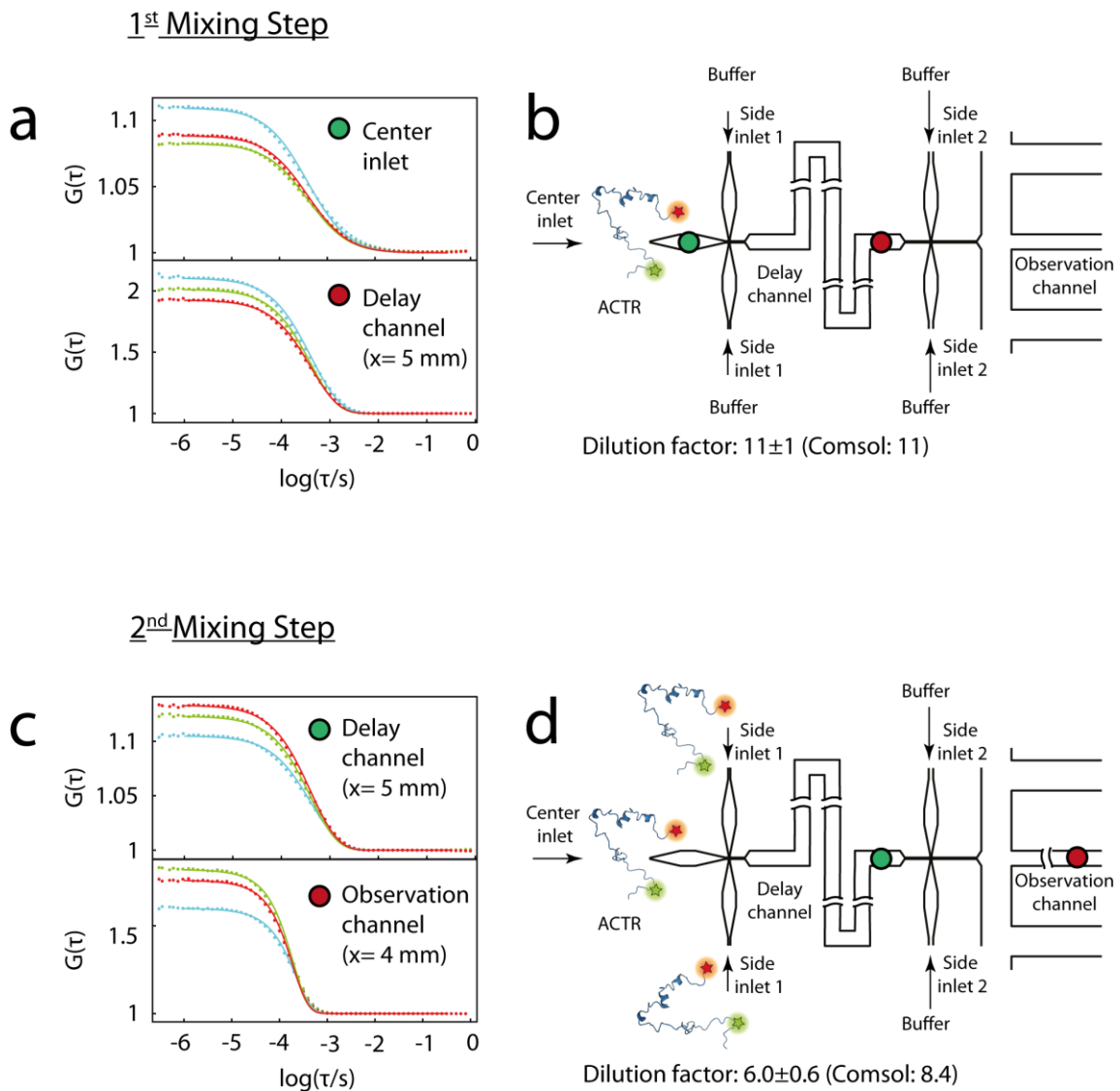
(a) The scanning electron micrograph shows an overview of both mixing regions, connected by the delay channel, and the beginning of the observation and outlet channels (scale bar: 100 μm). (b, c) Magnified view of the second mixing region (b) and the beginning of the observation channel (c). The widths of the delay channel and the observation channel were measured to be 48.3 μm and 48.4 μm , respectively, close to the designed width of 50 μm (scale bars: 20 μm).

Figure S3. Observed sample distribution after the second mixing step is in good agreement with finite-element calculations.



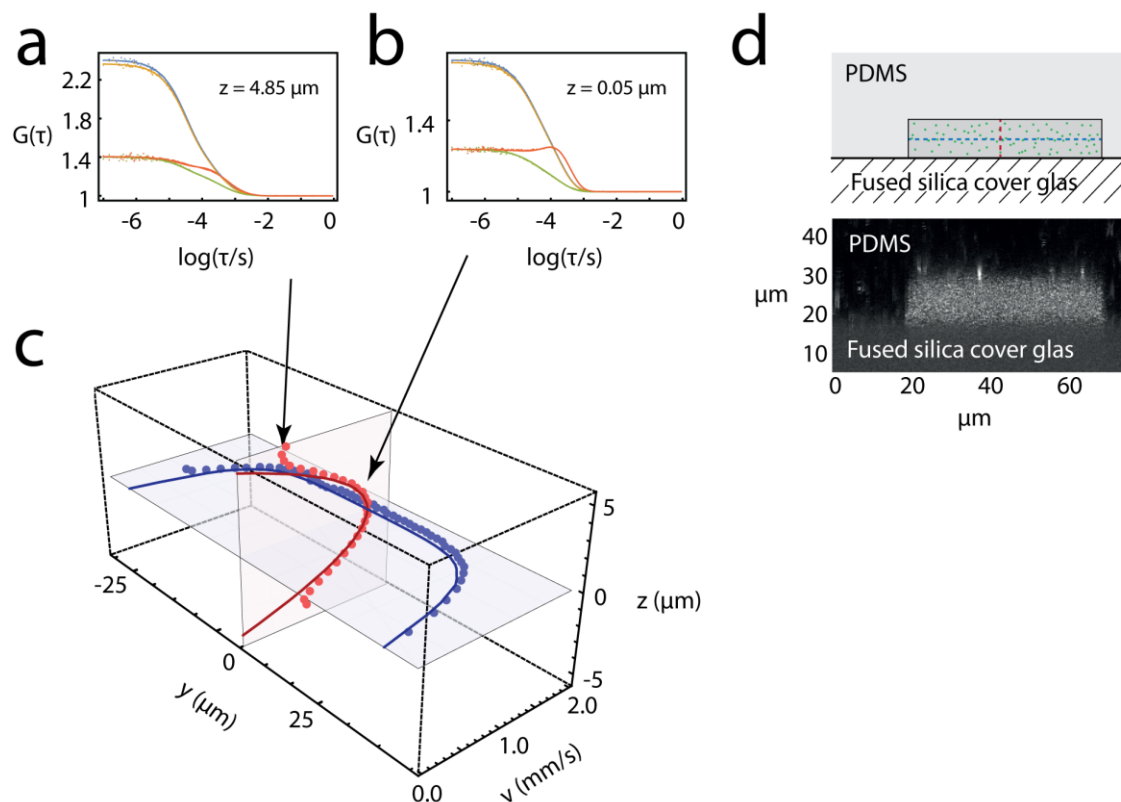
(a) Sample concentration after the second mixing step from finite-element calculations for a diffusion coefficient of 10^{-10} m^2/s for the sample molecules. The color gradient depicts the sample concentration on a logarithmic scale (inset) relative to an initial sample concentration of 1 in the center inlet. (b) Widefield fluorescence image of 20 kDa fluorescein-labeled dextran (~ 5 μM) diluted with buffer in the second mixing step. (c) Confocal scanning image of the end of the mixing neck, acquired during a typical single-molecule FRET measurement with fluorescently labeled ClyA. The sample molecules are hydrodynamically focused to a thin stream in the narrow mixing neck and start dispersing across the observation channel as they exit the mixing neck. The signal outside the channels originates from fluorescent impurities in the PDMS.

Figure S4. Characterization of mixing ratios using the amplitudes of fluorescence correlation functions.



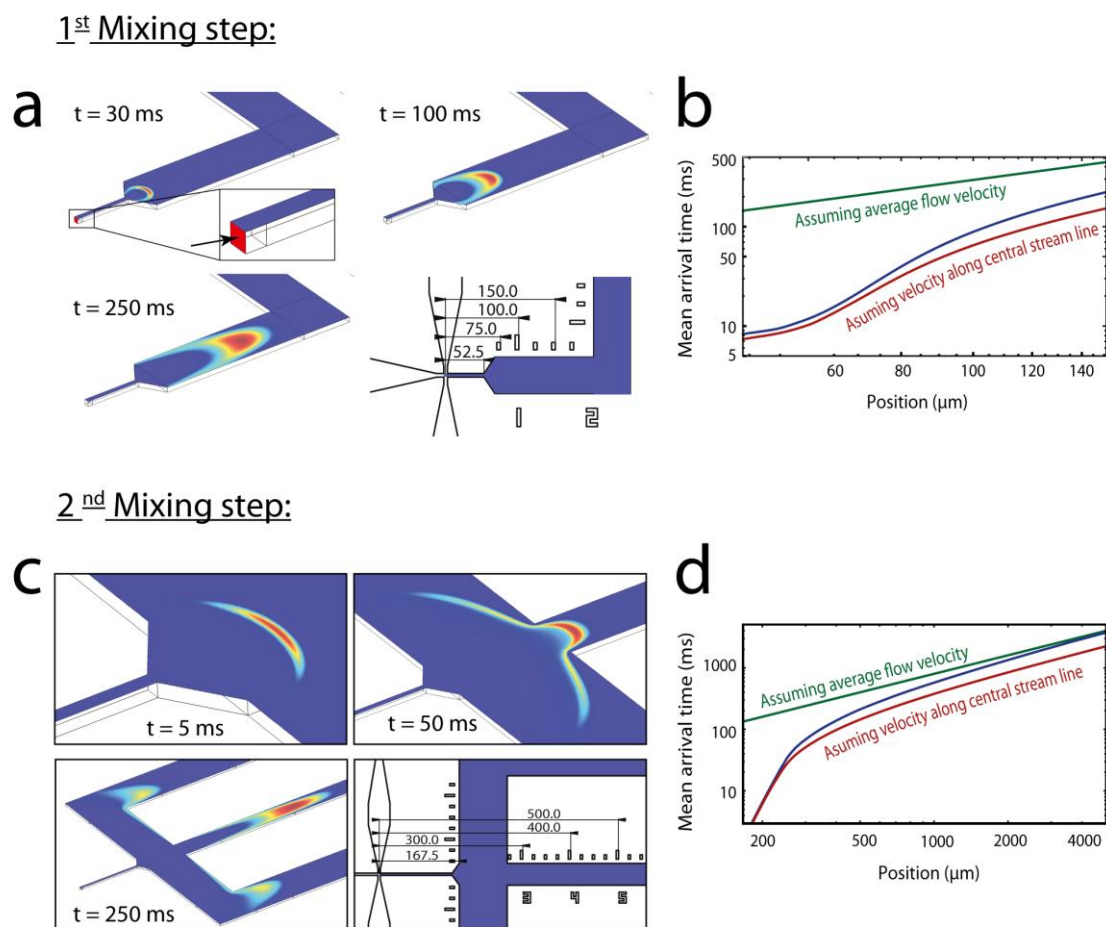
(a, c) Donor-acceptor cross-correlation curves of FRET-labeled ACTR measured at the positions indicated by colored circles in (b) and (d). The three colored cross-correlation curves shown for each position originate from measurements in three independent microfluidic devices to assess device-to-device variability. Donor- and acceptor-labeled ACTR (5 nM) is supplied from the center inlet and diluted with buffer from side inlets 1 and 2 to characterize the first mixing step (b). To determine the sample dilution after the second mixing step, labeled protein supplied at the same concentrations from the center inlet and the side inlets 1 is diluted with buffer from the side inlets 2 (d). For the fit of the donor-acceptor cross-correlation curves (shown as solid lines in (a) and (c)), the diffusion time is fixed based on an independent equilibrium measurement without flow (*Materials and Methods*). From the fit, the average number of molecules in the confocal volume is obtained, which is used to estimate the dilution factor. The error indicates the standard deviation from the three independent measurements. For the 1st mixing step, we find good, for the 2nd step reasonable agreement between the measured and calculated dilution factors.

Figure S5. Experimentally determined flow velocities are in good agreement with finite-element calculations.



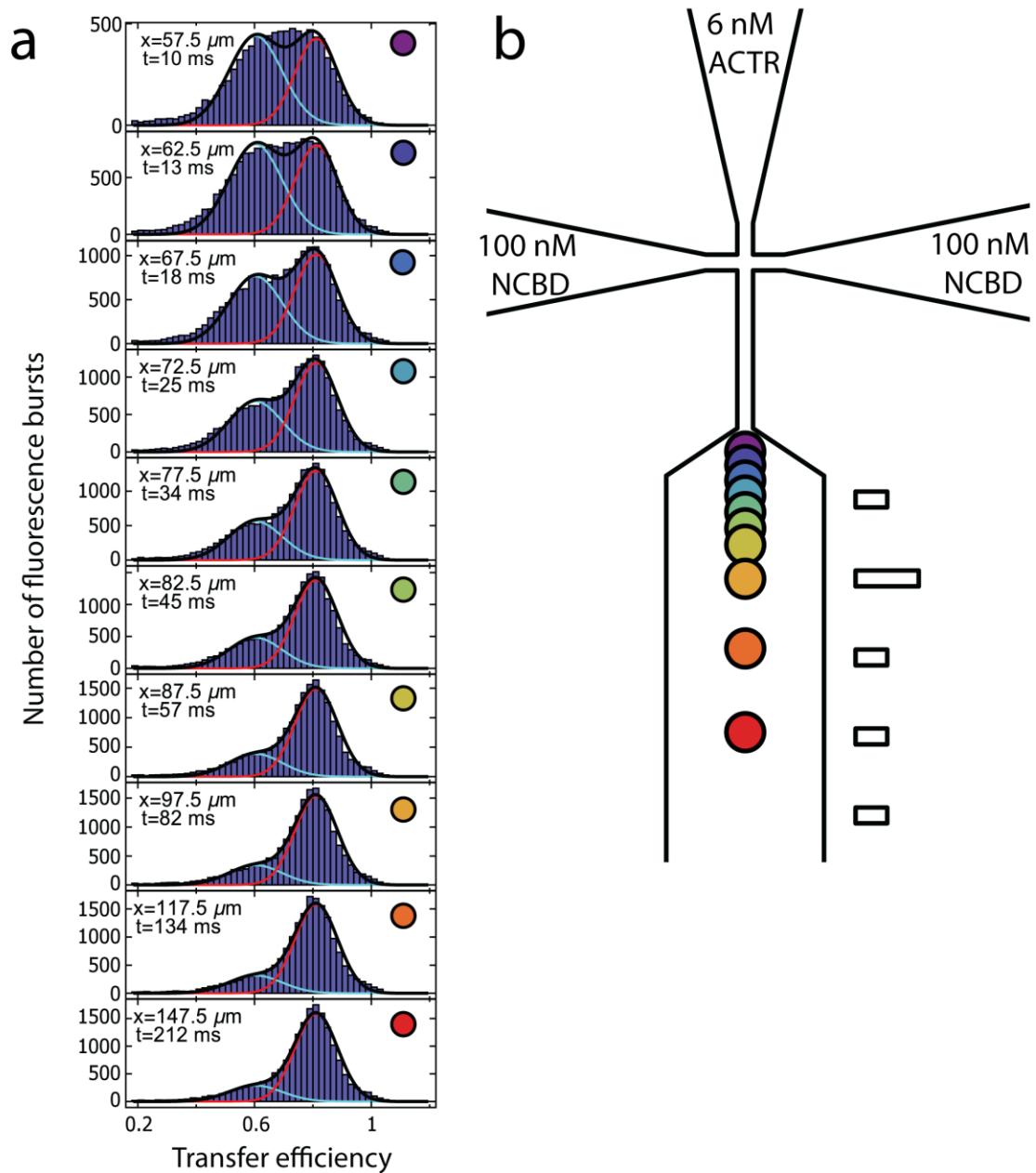
Flow velocities in the channels of the microfluidic device are characterized by two-focus FCS⁶. All inlet channels are filled with 0.7 nM of the fluorescent dye Alexa 488, and horizontal and vertical flow velocity profiles are determined 500 μm downstream of the second mixing region. Two representative sets of correlation curves are shown in (a) and (b). Displayed in blue and orange are the auto-correlations of the two foci; the cross-correlation curves between the foci are depicted in red (in direction of flow) and green (opposite to direction of flow). Flow velocities can be extracted from a global fit of the auto- and cross-correlation curves (solid lines)^{1, 6}. (c) Flow velocity profile in the z - (red data points) and y -direction (blue data points) from the two-focus FCS measurements. The solid lines are the flow-velocity profiles expected from 3D finite-element calculations. (d) Schematic representation of the cross-section of the observation channel filled with dye solution (top). The dashed lines indicate the planes along which the horizontal and vertical flow velocity profiles in (c) were measured. A corresponding fluorescence intensity scan is shown below.

Figure S6. Position-to-time conversion for accurately relating positions along the channels to times after mixing. (See also Videos S1 and S2.)



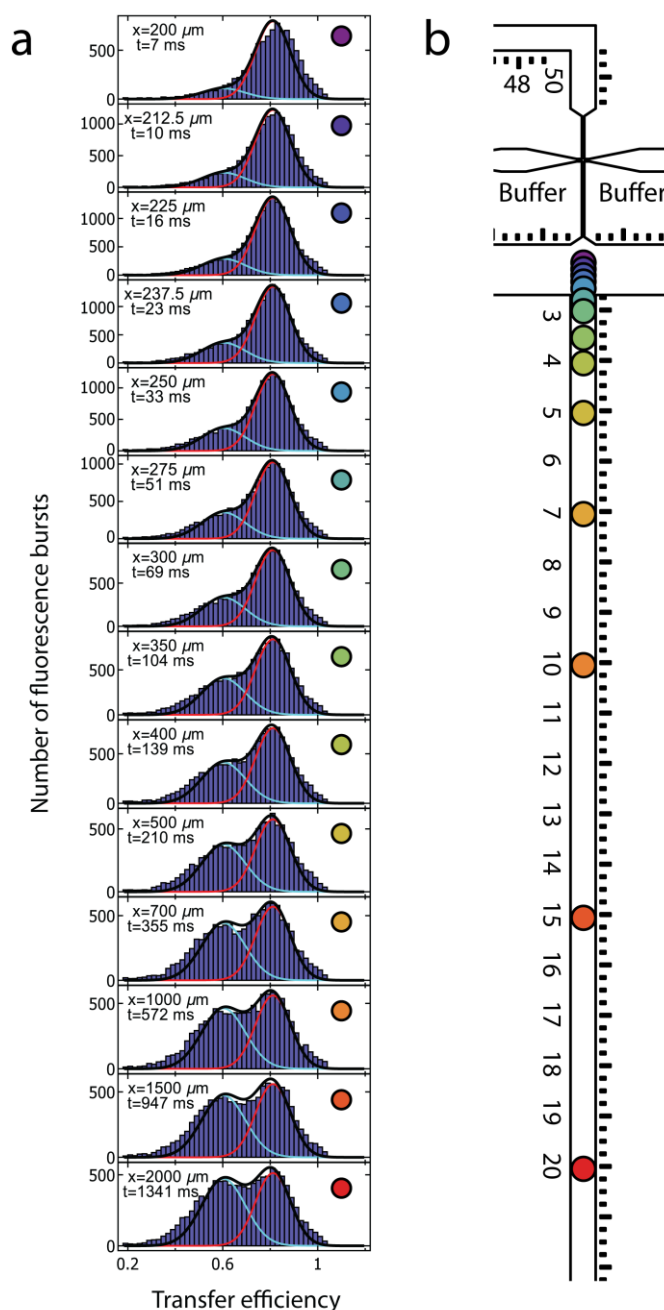
Time-resolved finite-element calculations of a narrow pulse of molecules (released at the junction of the corresponding inlet channels as indicated by the red square in (a)) are carried out to obtain conversion functions relating positions in the channels to the time after mixing that take into account Taylor dispersion¹. (a, c) Concentration profiles of sample molecules at different times after the first and second mixing steps, respectively. The color gradient indicates high concentrations in red and low concentrations in blue. The arrow in the inset in (a) indicates the boundary from which the pulse is released. (b, d) Mean arrival times from time-resolved finite-element calculations in blue, compared to the arrival times obtained for the two limiting regimes, either based on the average flow velocity across the channel (green) or the flow velocity along the central streamline (red). The resulting mean arrival time depends on the pressures applied to the inlet- and outlet-channels and the translational diffusion coefficient of the sample molecule¹. At early times (e.g. 30 ms after the first mixing step, (a)), the sample molecules are still focused to a thin stream and the arrival time can be obtained to good approximation using the flow velocity along the central streamline (red line). Due to diffusion perpendicular to the direction of flow, an increasing fraction of molecules samples stream lines with lower flow velocities for longer times after mixing, which leads to a broadening of the sample pulse (see, e.g., 250 ms after the first mixing step, (a)). For long times after mixing, where the molecules are homogeneously distributed across the channel, the average flow velocity (shown in green) can be used to determine the average arrival time at the position of the confocal volume¹. At intermediate times, a crossover between the two regimes occurs.

Figure S7. Time series of transfer efficiency histograms of donor- and acceptor-labeled ACTR upon binding to unlabeled NCBD measured after the first mixing step.



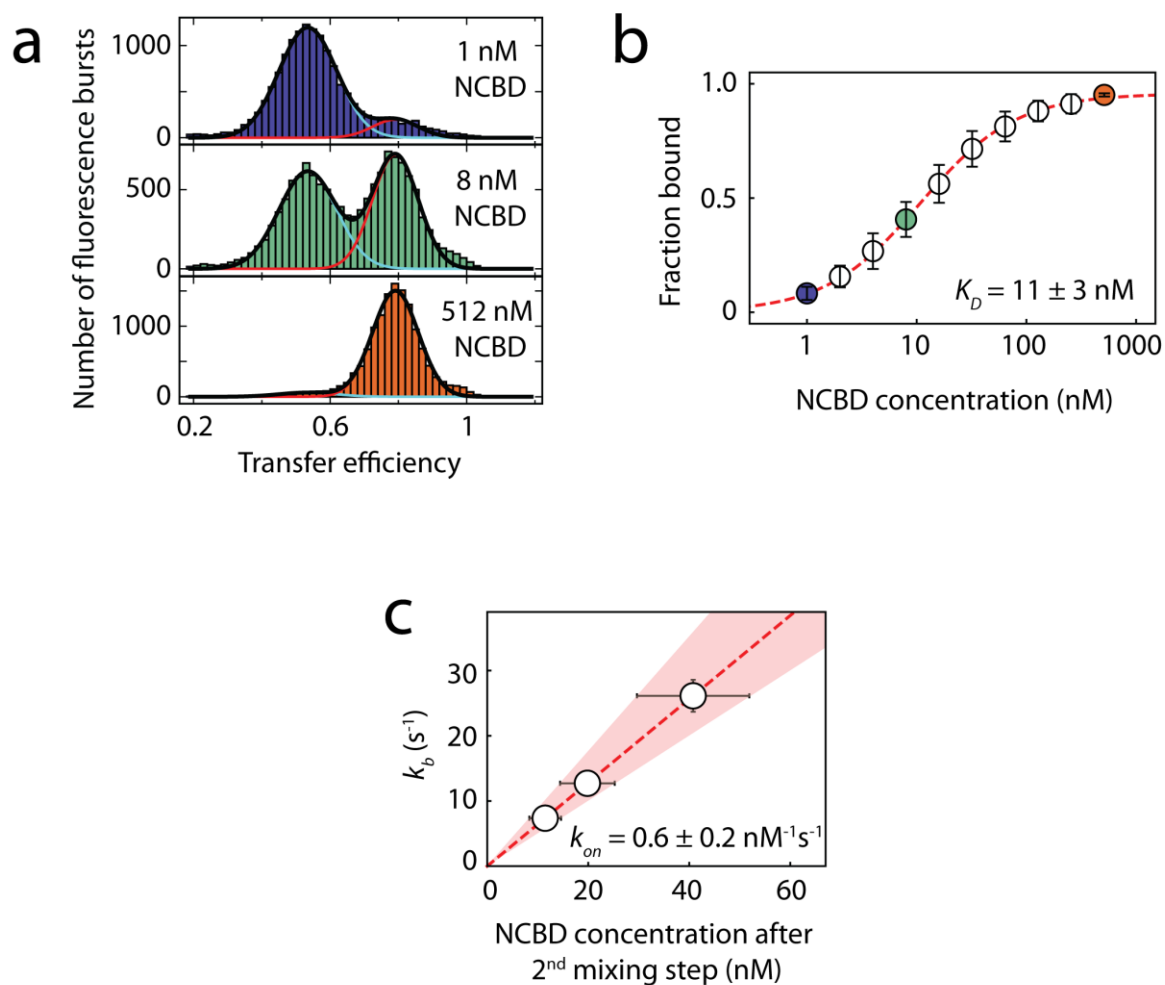
Donor- and acceptor-labeled ACTR (6 nM) is mixed with an excess of unlabeled NCBD (100 nM). (a) Histograms measured after the first mixing step, corresponding to one of the data sets shown in Figure 2, analyzed with a global fit of all histograms after the first and second mixing step (100, 200, and 400 nM NCBD). The low transfer efficiency peak ($\langle E \rangle = 0.60$) corresponds to unbound ACTR and the high transfer efficiency peak ($\langle E \rangle = 0.81$) to ACTR bound to NCBD. Over time, an increase in the fraction of bound ACTR is observed. For fitting, the ratio of the peak widths of both Gaussian peak functions are constrained to the value expected from the shot-noise limited peak widths at the respective mean transfer efficiencies. The positions and widths of the peaks are used as globally shared fit parameters. (b) Colored circles indicate the positions along the channel at which the transfer efficiency histograms were recorded.

Figure S8. Time series of transfer efficiency histograms of donor- and acceptor-labeled ACTR bound to unlabeled NCBD measured after the second mixing step, corresponding to dilution of the complex and the resulting dissociation.



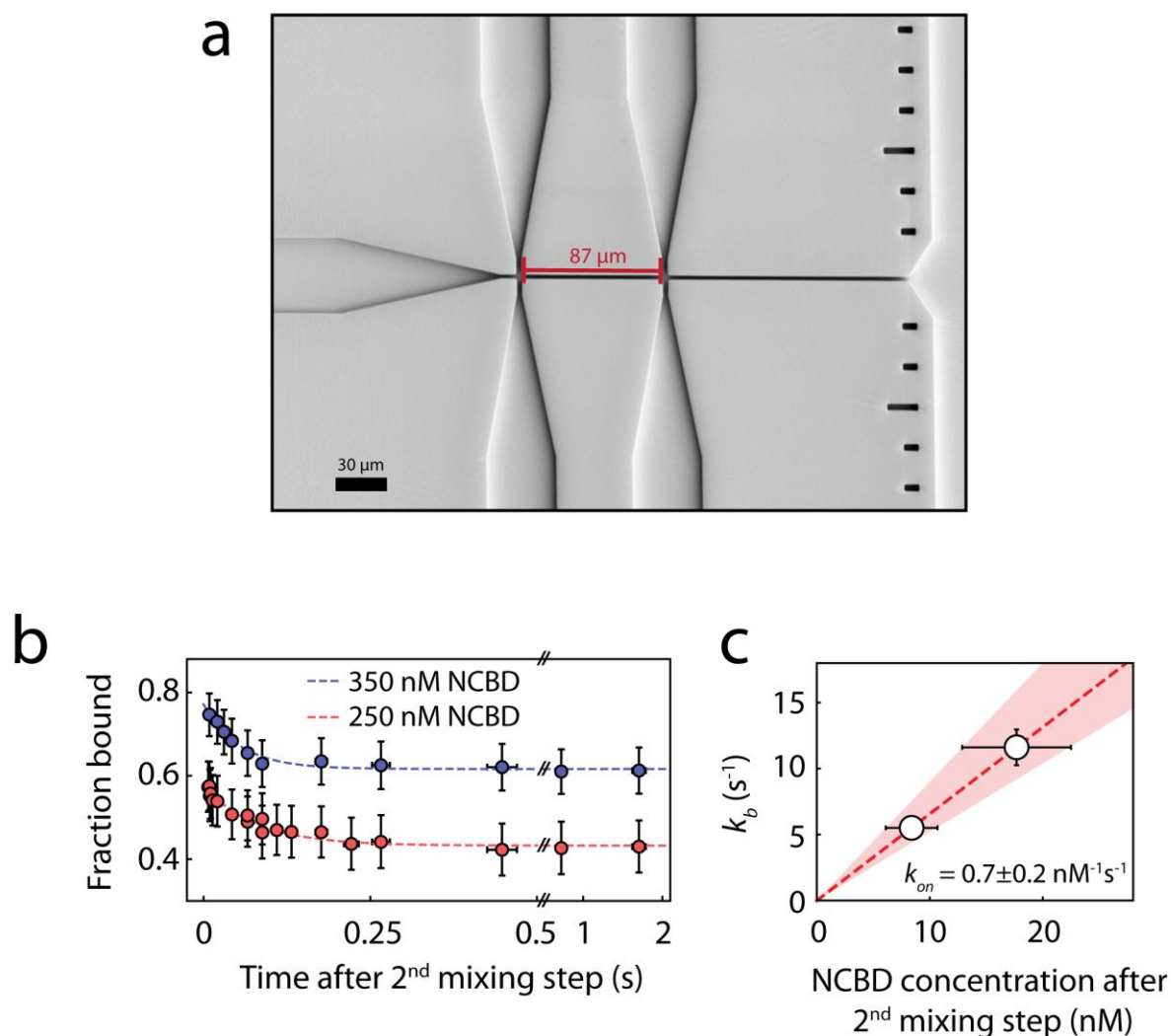
The ACTR/NCBD complex (formed after the first mixing step by mixing 6 nM donor- and acceptor-labeled ACTR with 100 nM unlabeled NCBD) is diluted with buffer (50 mM sodium phosphate, pH 7, 1mM β -mercaptoethanol, 0.01 % Tween 20) in the second mixing step, corresponding to one of the data sets shown in Figure 2. (a) Histograms recorded after the second mixing step (100 nM initial NCBD concentration), analyzed with a global fit of all histograms recorded after the first and second mixing step (100, 200, and 400 nM NCBD). For fitting, the procedure as described in caption of Figure S7 was applied. After dilution, the fraction of bound ACTR (high E) decreases until the equilibrium distribution is reached. (b) Colored circles indicate the positions along the channel at which the transfer efficiency histograms were recorded.

Figure S9. Affinity of ACTR to NCBD and association rate coefficient of the ACTR-NCBD complex.



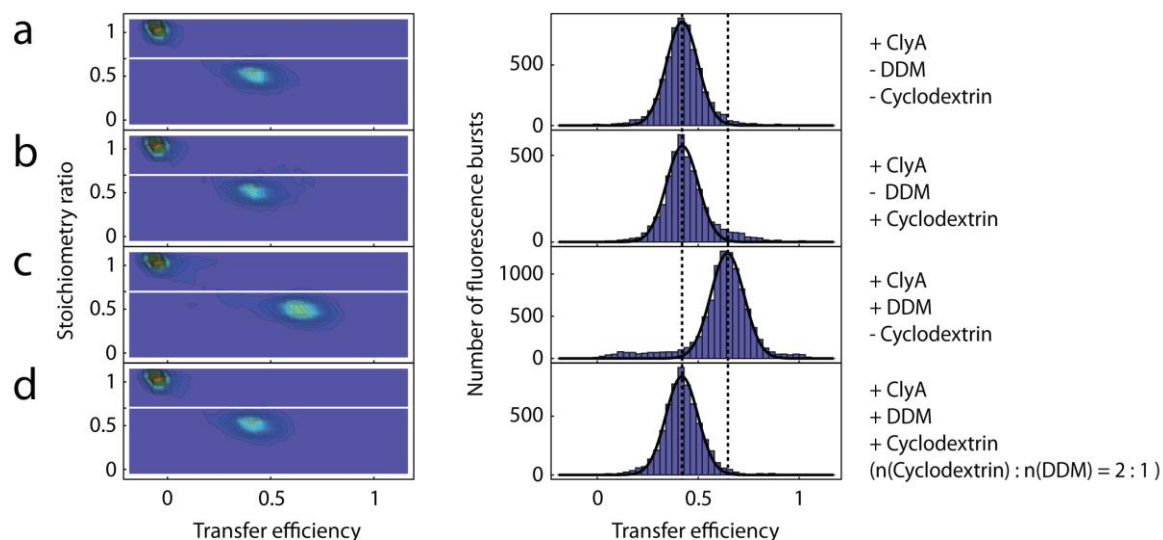
The dissociation constant (K_D) of the ACTR-NCBD complex was determined in an equilibrium titration experiment. A constant amount of donor- and acceptor-labeled ACTR (200 pM) is titrated with increasing amounts of NCBD (1 nM - 512 nM). (a) Examples of transfer efficiency histograms. (b) Binding isotherm based on the average of three independent measurements, with error bars representing standard deviations. The resulting K_D was used to determine the concentration of unlabeled NCBD in the observation channel from the fraction of bound ACTR at equilibrium, i.e., from the asymptotic value of the fit at long times (Figure 2c). (c) The apparent association rates (k_b) after the second mixing step were obtained from a global fit of the three datasets shown in Figure 2c. They are plotted against the NCBD concentration in the observation channel to determine the association rate coefficient, k_{on} . The shaded area indicates the uncertainty obtained by calculating the NCBD concentrations using a K_D of 8 and 14 nM, respectively, corresponding to the error bounds of K_D (b).

Figure S10. Association and dissociation rate coefficients of the ACTR/NCBD complex are unaffected if the complex is populated for only 25 ms using a short delay channel.



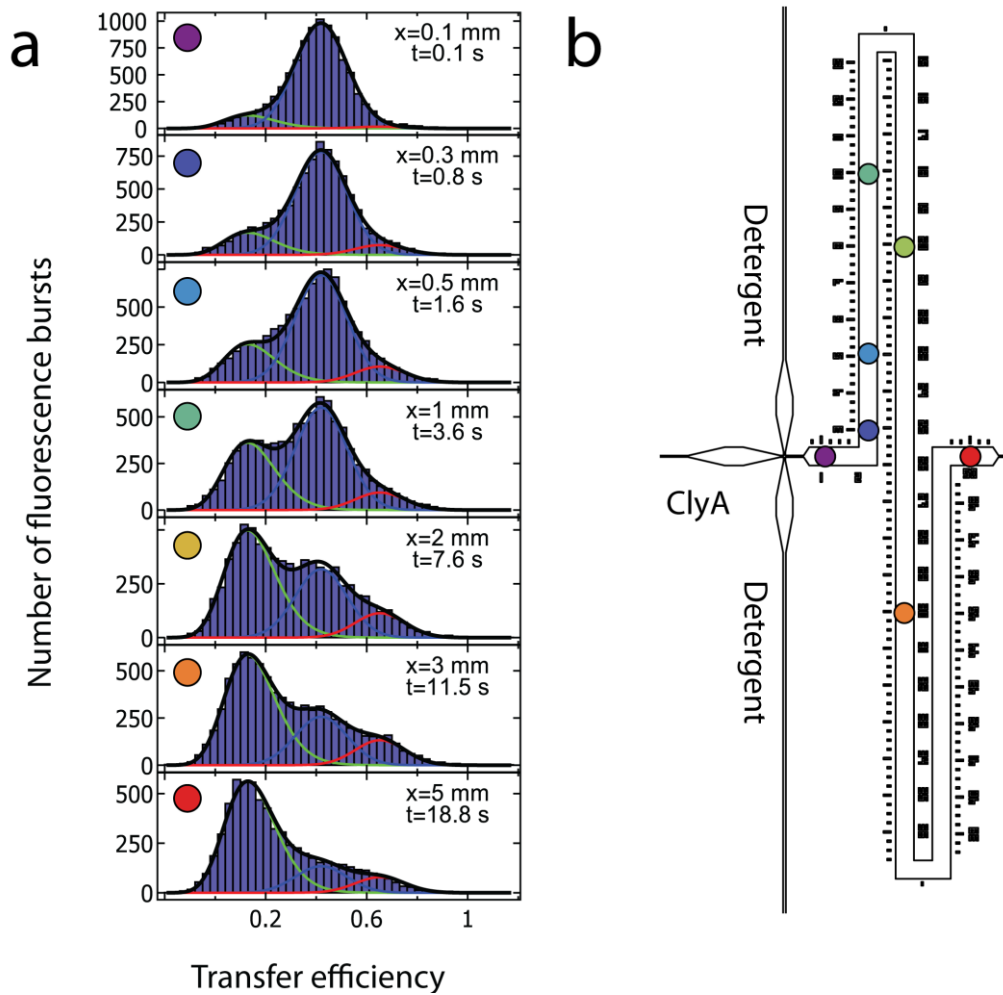
The association and dissociation rate coefficients of the ACTR/NCBD complex are unaffected if the complex is only populated for 25 ms, indicating that complex formation occurs without slowly formed kinetic intermediates. (a) Electron micrograph of the mixing regions of the microfluidic device used here, with the length of the delay channel reduced to 87 μm , corresponding to a delay time of 25 ms. (b) Dissociation kinetics measured after the second mixing step for two different NCBD concentrations (250 and 350 nM). Vertical error bars indicate the (largely systematic) uncertainties in the fraction bound from transfer efficiency histogram fitting. The dashed lines show a global fit assuming a 2-state process with a shared value for k_{off} ($7.2 \pm 0.9 \text{ s}^{-1}$) and two different apparent association rates, k_b . (c) The association rate coefficient, k_{on} , is estimated from the slope of a linear fit of k_b versus the NCBD concentration after the second mixing step (NCBD concentrations were quantified as described in Figure S9). The shaded area indicates the uncertainty obtained by calculating the NCBD concentrations using a K_b of 8 and 14 nM, respectively, the error bounds of the value (Figure S9b).

Figure S11. β -cyclodextrin does not influence the conformation of ClyA.



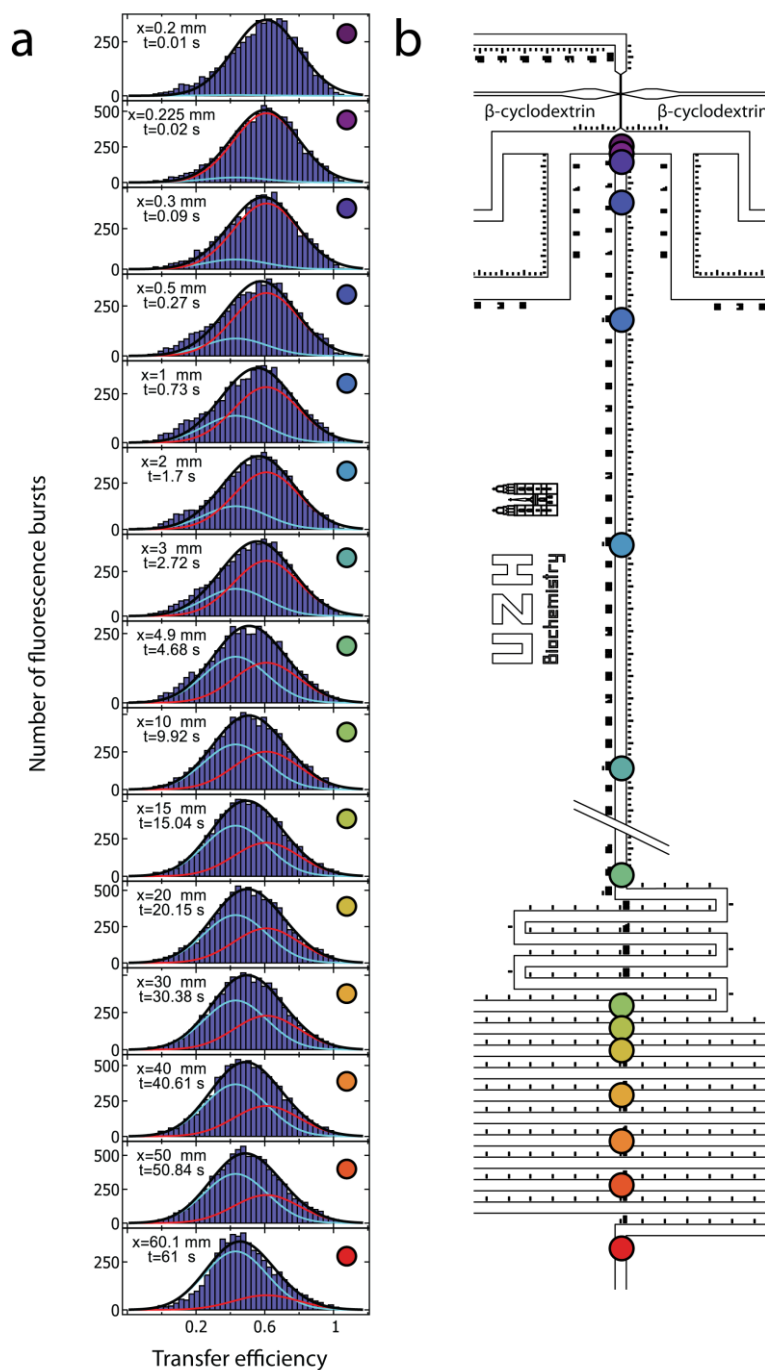
Equilibrium transfer efficiency histograms of ClyA (25 mM sodium phosphate, 75 mM NaCl, pH 7, 144 mM β -mercaptoethanol, 0.001 % Tween 20) in the presence and absence of 4 mM β -cyclodextrin are in good agreement (a, b), indicating that the conformation of ClyA is unaffected by β -cyclodextrin. Data were recorded with pulsed-interleaved excitation¹² to remove the donor-only population originating from molecules lacking an active acceptor dye. Only fluorescence bursts with a stoichiometry ratio of less than 0.7 were selected for the histograms displayed on the right (see *Materials and Methods* for details). (c) Upon addition of 2 mM (\sim 0.1 % (w/v)) n-dodecyl β -D-maltoside (DDM), ClyA undergoes a characteristic conformational change that results in a shift of the transfer efficiency². (d) Measurements where DDM is incubated with β -cyclodextrin in a 1:2 stoichiometric ratio (4 mM β -cyclodextrin and 2 mM DDM) and ClyA added subsequently yield a transfer efficiency histogram indistinguishable from the one measured without detergent (a), showing that DDM is sequestered quantitatively by β -cyclodextrin.

Figure S12. Global fit of a time series of transfer efficiency histograms of donor- and acceptor-labeled ClyA upon binding DDM.



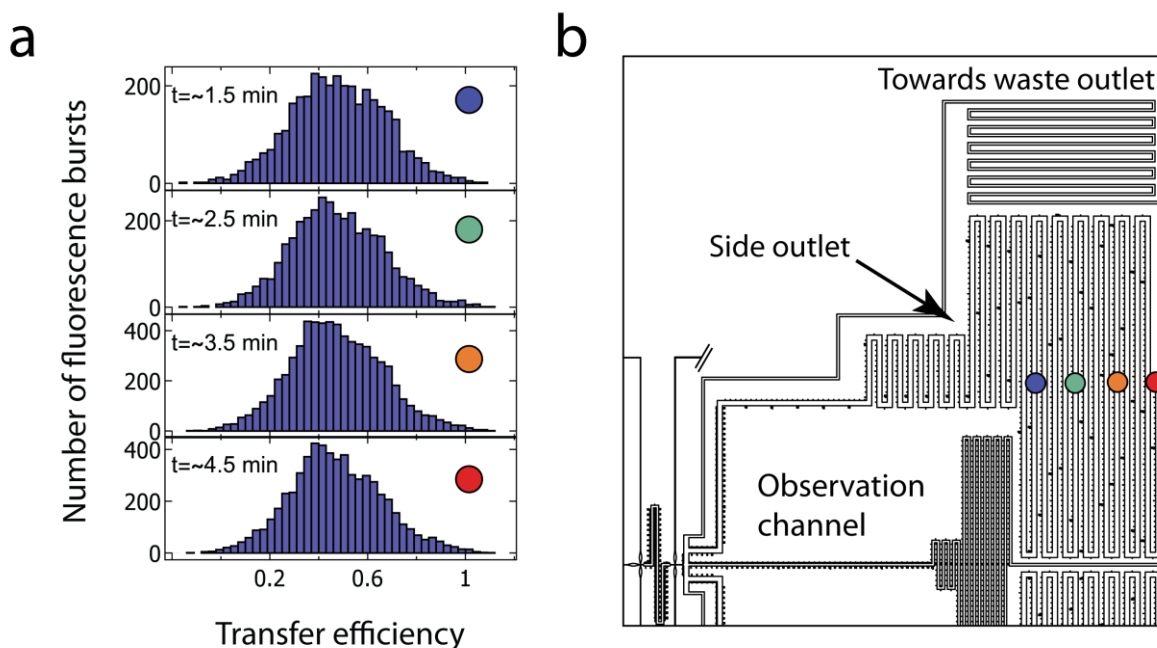
Donor- and acceptor-labeled ClyA (15 nM) is mixed with a 0.11 % (w/v) solution of the detergent DDM to induce the formation of the intermediate state observed during protomer formation of the protein². (a) Global fit of a time series of transfer efficiency histograms measured after the first mixing step. The low transfer efficiency peak ($\langle E \rangle = 0.13$), corresponding to the intermediate, is described by a lognormal peak function. The populations of the ClyA monomer ($\langle E \rangle = 0.42$) and the protomer ($\langle E \rangle = 0.65$) are fitted with a Gaussian peak function. The width of the high transfer efficiency population is constrained to 0.098, the value obtained in previous microfluidic mixing experiments². (b) Colored circles indicate the positions along the delay channel where the transfer efficiency histograms were recorded.

Figure S13. Time series of transfer efficiency histograms of donor- and acceptor-labeled ClyA measured after the second mixing step, where the detergent is sequestered by mixing with β -cyclodextrin.



Starting from the intermediate state populated after the 1st mixing step (Figure S12), β -cyclodextrin is added in the 2nd mixing step to sequester DDM. (a) Global fit of a series of transfer efficiency histograms recorded at the positions and times after mixing indicated in the panels. The position ($\langle E \rangle = 0.61$) and width (0.2) of the high transfer efficiency peak is constrained to the values obtained from fitting the first transfer efficiency histogram. The position and width of the low transfer efficiency peak are globally shared fit parameters, resulting in values of 0.43 and 0.18, respectively. (b) Colored circles indicate the positions along the delay channel where the transfer efficiency histograms were recorded.

Figure S14. Time series of transfer efficiency histograms of donor- and acceptor-labeled ClyA measured up to 4.5 minutes after the second mixing step in the additional observation channel.

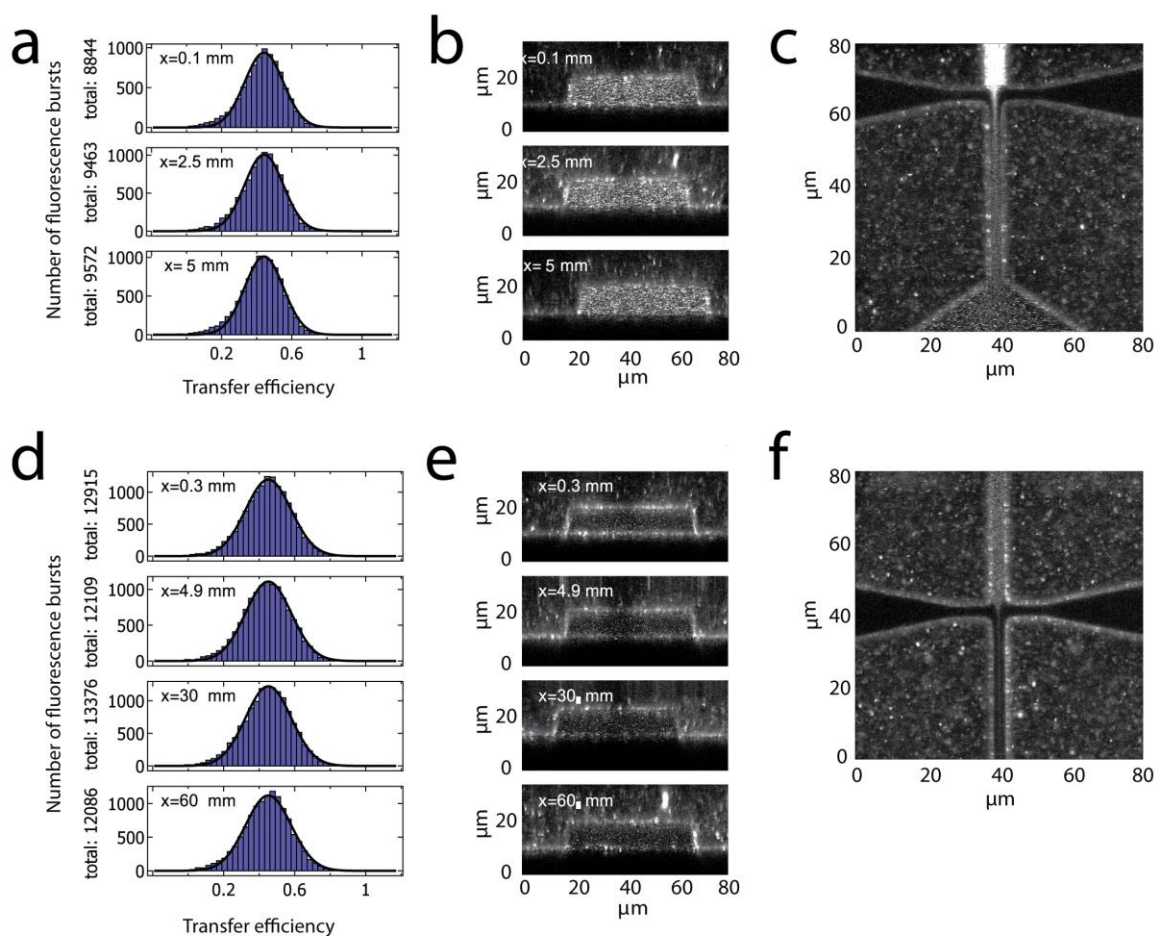


Times up to 4.5 minutes after the second mixing step are accessible by measuring in the side outlet channel. (a) Time series of transfer efficiency histograms measured at the indicated times after mixing ClyA in 0.1 % (w/v) DDM with β -cyclodextrin. Note that the peak widths of the transfer efficiency histograms measured in the microfluidic device are increased compared to measurements in free diffusion (see Fig. 3b “Manual mixing”). This is a consequence of the reduced residence times of the molecules drifting through the confocal volume compared to measurements in the absence of flow, which results in shorter bursts and therefore increased shot noise broadening of the histograms (b) Colored circles indicate the positions along the additional observation channel where the transfer efficiency histograms were recorded.

Table S1. Steady-state anisotropies of the donor and acceptor dye (Alexa 488 and 594) in the ClyA time series after the second mixing step (Figure S13). Anisotropy values do not change significantly during the reaction. Slow orientational relaxation of the fluorophores can thus be excluded as a dominant source of the pronounced broadening of the transfer efficiency histograms in the compact unfolded state¹⁴.

| Position from 2 nd mixing neck (mm) | Time after mixing (s) | Donor anisotropy (Alexa 488) | Acceptor anisotropy (Alexa 594) |
|--|-----------------------|------------------------------|---------------------------------|
| 0.2 | 0.008 | 0.15 | 0.20 |
| 0.225 | 0.02 | 0.16 | 0.20 |
| 0.3 | 0.09 | 0.16 | 0.21 |
| 0.5 | 0.3 | 0.16 | 0.20 |
| 1 | 0.7 | 0.17 | 0.20 |
| 2 | 1.7 | 0.16 | 0.20 |
| 3 | 2.7 | 0.16 | 0.20 |
| 4.9 | 4.7 | 0.17 | 0.20 |
| 10 | 9.9 | 0.17 | 0.19 |
| 15 | 15.0 | 0.17 | 0.18 |
| 20 | 20.2 | 0.16 | 0.19 |
| 30 | 30.4 | 0.17 | 0.18 |
| 40 | 40.6 | 0.17 | 0.19 |
| 50 | 50.8 | 0.17 | 0.19 |
| 60.1 | 61.0 | 0.17 | 0.18 |

Figure S15. Nonspecific surface interaction of donor- and acceptor-labeled ClyA with channel walls is independent of position along the channel.



Characterizing nonspecific surface interaction of fluorescently labeled ClyA with the channel walls after the first (a-c) and second (d-f) mixing step. The number of detected bursts is constant along the delay- and observation channel, indicating that there is no progressive loss of sample molecules due to surface interactions (a and d). Note that the transfer efficiency histograms are slightly broadened after the second mixing step. This is due to a decreased signal-to-noise ratio, owing to the higher flow velocity and thus less bright bursts compared to measurements after the first mixing step. Intensity scans of the cross section of the delay- and observation channels (b and e) show no increased brightness of the channel walls as a function of channel position. (c and e) Intensity scans of the first (c) and second (f) mixing step.

References:

- (1) Wunderlich, B.; Nettels, D.; Schuler, B., *Lab Chip* **2014**, *14*, 219.
- (2) Benke, S.; Roderer, D.; Wunderlich, B.; Nettels, D.; Glockshuber, R.; Schuler, B., *Nat. Commun.* **2015**, *6*, 6198.
- (3) Taylor, G., *Proc. R. Soc. London, Ser. A* **1953**, *219*, 186.
- (4) Wunderlich, B.; Nettels, D.; Benke, S.; Clark, J.; Weidner, S.; Hofmann, H.; Pfeil, S. H.; Schuler, B., *Nat. Protocols* **2013**, *8*, 1459.
- (5) Magde, D.; Webb, W. W.; Elson, E. L., *Biopolymers* **1978**, *17*, 361.
- (6) Arbour, T. J.; Enderlein, J., *Lab Chip* **2010**, *10*, 1286.
- (7) Hofmann, H.; Soranno, A.; Borgia, A.; Gast, K.; Nettels, D.; Schuler, B., *Proc. Natl. Acad. Sci. USA* **2012**, *109*, 16155.
- (8) Schilling, J.; Schöppe, J.; Plückthun, A., *J. Mol. Biol.* **2014**, *426*, 691.
- (9) Cull, M. G.; Schatz, P. J., Biotinylation of proteins in vivo and in vitro using small peptide tags. In *Methods Enzymol.*, Academic Press: 2000; 430.
- (10) Altman, R. B.; Terry, D. S.; Zhou, Z.; Zheng, Q.; Geggier, P.; Kolster, R. A.; Zhao, Y.; Javitch, J. A.; Warren, J. D.; Blanchard, S. C., *Nat. Methods* **2012**, *9*, 68.
- (11) Soranno, A.; Koenig, I.; Borgia, M. B.; Hofmann, H.; Zosel, F.; Nettels, D.; Schuler, B., *Proc. Natl. Acad. Sci. USA* **2014**, *111*, 4874.
- (12) Müller, B. K.; Zaychikov, E.; Bräuchle, C.; Lamb, D. C., *Biophys. J.* **2005**, *89*, 3508.
- (13) Kudryavtsev, V.; Sikor, M.; Kalinin, S.; Mokranjac, D.; Seidel, C. A.; Lamb, D. C., *ChemPhysChem* **2012**, *13*, 1060.
- (14) Hillger, F.; Hänni, D.; Nettels, D.; Geister, S.; Grandin, M.; Textor, M.; Schuler, B., *Angew. Chem. Int. Ed.* **2008**, *47*, 6184.